Geochimica et Cosmochimica Acta xxx (xxxx) xxx

Contents lists available at ScienceDirect

Geochimica et Cosmochimica Acta

journal homepage: www.elsevier.com/locate/gca

Experimental pathways of clay formation and kinetics of basalt alteration in poor drainage systems: Implications for weathering

Piyush Sriwastava [a,b], Vijay Kumar Saini [a,c], George Mathew [a,*], Anil D. Shukla [d]

[a] Department of Earth Sciences, Indian Institute of Technology Bombay, Mumbai, Maharashtra 400076, India
[b] Museum of Natural History, University of Oxford, Parks Road, Oxford OX1 3PW, UK
[c] Helmholtz-Zentrum Dresden-Rossendorf e. V.- Institute of Resource Ecology, Bautzner Landstraße 400, 01328 Dresden, Germany
[d] Physical Research Laboratory, Ahmedabad, Gujarat 380059, India

ARTICLE INFO

Associate editor: Alexis Navarre-Sitchler

Keywords:
Basalt Weathering
Enhanced Rock weathering
Carbon Dioxide Removal
Clays
Dissolution kinetics

ABSTRACT

Basalt being the most dominant rock on the earth's crust, contributes significantly to the global elemental cycle through weathering. In recent years, the potential of basalt weathering has been continuously scrutinized as a carbon dioxide removal (CDR) strategy. An accurate estimation of such large-scale processes requires a deeper insight into the mechanism controlling the basalt glass dissolution under field conditions. This contribution assesses the chemical evolution of fluid interacting with basalt glass in poorly drained regimes. Experiments showed a drop in kinetics of alteration ($r_0 = 1.7 \times 10^{-9}$ mol.m^{-2}. s^{-1}) by two orders of magnitude in 24 days and emphasizes the onset of secondary mineral formation within 20 hr of the start of dissolution. At first, Mg starts fractionating from the solution due to brucite oversaturation and reaches undersaturation after 60th hour due to onset of other Mg-bearing minerals. From the 54th hour, montmorillonite remains oversaturated until Mg is entirely consumed by precipitation at the 164th hour. SEM-EDS investigation shows the presence of two major morphologies of secondary products: (a) honeycomb shape (smectite), with high Mg (>3 wt%) and octahedral composition similar [(Si/Al + Fe + Mg) and Al/Si] to smectite, (b) aggregate of ellipsoid and/or equant granular phases. Compositionally, elliptical and granular aggregates show affinity towards low Mg and high Fe variety of smectite amorphous precursor. The absence of pure brucite grains indicates epitaxial growth of Mg-rich, honeycomb-shaped phyllosilicate precursor on the brucite template due to well-reported structural similarity between the brucite layer and 2:1 phyllosilicate octahedral sheet. Elliptical and equant-shaped grains with or without compositional similarity with smectite phases have high Fe and low Mg, indicating their formation under a low Mg concentration stage in solution. Precipitation of the secondary phases at various stages of reaction progress affects the total reaction affinity in a closed system. Coupled dissolution and precipitation at the fluid-rock interface are responsible for lowering the kinetics of dissolution reactions in a closed system, previously explaining the slow kinetics of natural weathering regimes. The damped kinetics of dissolution and cations fractionation in secondary products within a few hours of onset of dissolution reaction can result in an overestimation (ten times) of CDR potential estimation by enhanced rock weathering (ERW) if calculations do not involve the nature of closed system evolution during basalt glass alteration.

1. Introduction

Silicate weathering, viz., disintegration and decomposition of rock, drives the element cycle on earth surface (Frings and Buss, 2019). Ions released during chemical weathering have two crucial fates: (1) carried away by river from catchment or (2) captured in neoformed secondary minerals, e.g., clays, carbonates or metal (oxy)hydroxide (Velde and Meunier, 2008), that are vital for organisms nutrient turnover (Fang et al., 2023). Rivers in basaltic terrain have shown the highest cationic flux due to highly reactive constituents in basalt such as amorphous interstitial glass, pyroxene and olivine (Eggleton et al., 1987; Nesbitt and Wilson, 1992; Hermanska et al., 2023) resulting 30 – 35 % of global CO_2 fixation in the form of bicarbonates of cations, that later lead to carbonate precipitation (Dessert et al., 2003). The dominant pathway of carbon dioxide removal (CDR) by weathering of basalt can be expressed by chemical reaction:

* Corresponding author.
E-mail address: gmathew@iitb.ac.in (G. Mathew).

https://doi.org/10.1016/j.gca.2025.01.042
Received 23 April 2024; Accepted 30 January 2025
Available online 31 January 2025

$$CaSiO_3 + 2CO_2 + 3H_2O \rightarrow Ca^{+2} + 2HCO_3^- + H_4SiO_4 \quad (1)$$

Basalt weathering has not only significant control over the long-term CO_2 content in atmosphere but also on global cycle of elements and chemistry of earth's critical zone (Kump et al., 2000; Dessert et al., 2001; Stefansson and Gislason, 2001). The rate of CO_2 fixation can be increased by enhanced kinetics of basalt dissolution (Schuiling and Krijgsman, 2006), which is achieved by addition of finely crushed basalt (Goll et al., 2021; Rinder and Hagke, 2021; Vienne et al., 2022). Beerling et al. (2020), Strefeler et al. (2018) and Taylor et al. (2016) have demonstrated that enhanced weathering of basaltic rock can be adopted as potential CO_2 removal strategies as it can capture 10.5 ± 3.8 t CO_2 ha^{-1} (Beerling et al., 2024) if applied in croplands which also enhances the food security and crop productivity. According to reaction (1), the large-scale estimation of CDR potential will directly depend on bivalent cations supply rate and residence time, which depend on the kinetics of basalt dissolution and proximity of the system to equilibrium or precipitation conditions, respectively. Most large-scale calculations are based on basalt dissolution models under open systems, which are far from equilibrium. Natural weathering in near-surface environments is dominated by poor drainage systems, where fluid leads to coupled dissolution and precipitation at the fluid-rock interface.

Numerous studies have been done to understand initial basalt dissolution kinetics over a wide range of temperatures and pH in an open system (e.g. Gislason and Eugster, 1987a; Guy and Schott, 1989; Crovisier et al., 1988a, 1988b, 1990, 1992, 2003; Daux et al., 1994, 1997). Oelker and Gislason (2001) and Heřmanská et al. (2023) have proposed an empirical formula to calculate the steady state rate (r) of basalt glass dissolution in an open system, far from the equilibrium. However, basalt dissolution in a closed system remains less probed. Daux et al. (1997) studied basalt dissolution kinetics evolution using multiple open systems with high flow rates resulting far from equilibrium systems and low flow rates resulting near equilibrium systems analogous to closed systems. Following transition state theory, the steady-state rate of each reaction setup strongly correlated with reactions Gibbs free energy (ΔG_r). Techer et al. (2001) investigated the general dissolution model based on TST to explain the basalt dissolution kinetics in a closed system approaching equilibrium. However, the relationship between kinetic evolution and total chemical affinity remains unexplained. Although closed systems kinetics evolution has been understood for minerals like alkali feldspar with coupled dissolution-precipitation during alteration reaction in a closed system (Alekseyev et al., 1997; Zhu and Lu, 2009; Zhu et al., 2010), such an approach requires a mechanistic understanding for basaltic glass.

According to current understanding, basalt interaction with water starts with H_2O diffusion and hydration of a silicate network followed by a metal proton exchange reaction, resulting in a hydrated glass layer (Bourcier et al., 1992; Angeli et al., 2006). Initially, the diffusion rate is higher than the hydrolysis rate; eventually, with increasing thickness of the hydrated glass layer, diffusion rates slow down to the hydrolysis rate, and the dissolution reaction becomes congruent (Gislason and Eugster, 1987; Crovisier., 1992). Hydrolysis at higher temperatures occurs partially, resulting in a porous surface layer facilitating diffusion (Berger et al., 1987, 1988, 1994), while hydrolysis is total at low temperatures. Neeway et al. (2016) have proposed an alkali interdiffusion model based on Fick's law for quantitatively constraining the diffusion parameters. Bouakkaz et al. (2016) studied glass (SON68) dissolution in an open system (flow-through reactor) using ^{29}Si doped fluid and showed that both diffusion and surface alteration reactions govern glass dissolution. Bouakkaz and others reported that the hydrated glass layer is Mg-poor. Secondary products are Mg-rich silicates, indicating a unique role of Mg during glass alteration reaction, as envisaged in the present work. Since basalt dissolution kinetics is controlled by surface reactions (Berner, 1978; Murphy et al., 1989), many researchers have attempted to establish a general relation between reaction rates and chemical affinity under Transition State Theory (TST), considering the desorption of different surface complexes as a rate-defining step. Grambow (1985) considered desorption of purely siliceous surface complex as a rate-defining step and proposed first-order rate law, which is a function of proton activity in solution [H^+] and activity of orthosilicic acid [H_4SiO_4]. Berger et al. (1994) considered =SiOH as a precursor species, and the basalt dissolution rate was a function of 0.33 power of Q/K, where Q is precursor species activity, and K is amorphous silica hydrolysis reaction's solubility constant. The power value (0.33) in this rate calculation equation depends on the silica retention amount in the alteration gel, which varies with temperature. Daux et al. (1997) studied the dissolution kinetics of basalt at 90 °C and considered hydrolysis of a hydrated glass layer with composition Si, Al, Fe and H_2O as a determining step. Although numerous attempts have been made to unveil the mechanism of basalt dissolution and establish kinetics relations in an open system, the fate of ions released in a closed system needs investigation from the perspective of kinetics evolution, the effect of equilibrium on kinetics and pathways of secondary mineral formation.

Hence, the current study has investigated the pathways of basalt glass alteration in alkaline conditions under a closed system as water bodies in basaltic terrain become alkaline (Gislason et al., 1996; Reimers et al., 1996; Dessert et al., 2001; Pokrovsky et al., 2005). We have used basalt glass rather than a crystalline rock for two reasons: (1) each crystallised basalt contains variable amounts of interstitial glass and crystalline components. The dissolution rate of glass being faster than crystalline controls the pathways of precipitation reaction, (2) to bridge the knowledge gap of glass dissolution mechanism and kinetics, which is crucial for reaction path modelling of normal basalt in which the crystalline components, e.g., pyroxene and plagioclase have been well understood.

In the present contribution, we have evaluated the following two problems associated with basalt glass alteration in closed-system that hold importance from the perspective of a new strategy of CDR using ERW of basalt glass: 1) Evolution of alteration kinetics, ΔG_r and pathways of secondary mineral formation in a closed alkaline system and 2) The disparity between dissolution rate estimation and total reaction affinity in a closed system following TST, explained by coupled dissolution and precipitation reactions. We have also estimated the impact of poor drainage conditions on CDR potential.

2. Material and Methods

2.1. Sample preparation

The basalt glass used in this study is a natural glass collected from Hawaii Island. It was ground using agate mortar to increase the reactive surface area. The ground sample was sieved to obtain 36–56 μm and less than 36 μm size fraction. The 36 –56 μm fraction was cleaned with ultrasonic bath to remove the ultra-fine particles. First, cleaning was done for 10 min in deionised water, followed by acetone. Five to six cleaning cycles with water and acetone were sufficient to remove all fine particles from 36–56 μm fraction. Subsequently, the sample was dried overnight at 60 °C.

2.2. Experiment Setup

The experiment was performed in a custom-made setup (Fig. 1). A closed four-necked round bottom flask was equipped with a temperature sensor probe connected to the solution and a PID controller. The flask was kept on a heating mantle, having a rounded opening with woven fabric in the surroundings, to heat homogeneously. The heater system and PID controller were synced to maintain the system's temperature within the ± 1°C range. A mechanical stirrer was employed in the reaction setup to keep the reacting grains of basalt glass in suspension throughout the reaction. There was a retractable outlet system and a PTFE syringe of 5 ml connected with a flexible teflon pipe. 1.25 ml of the solution was piped out at regular intervals. Each sample was filtered

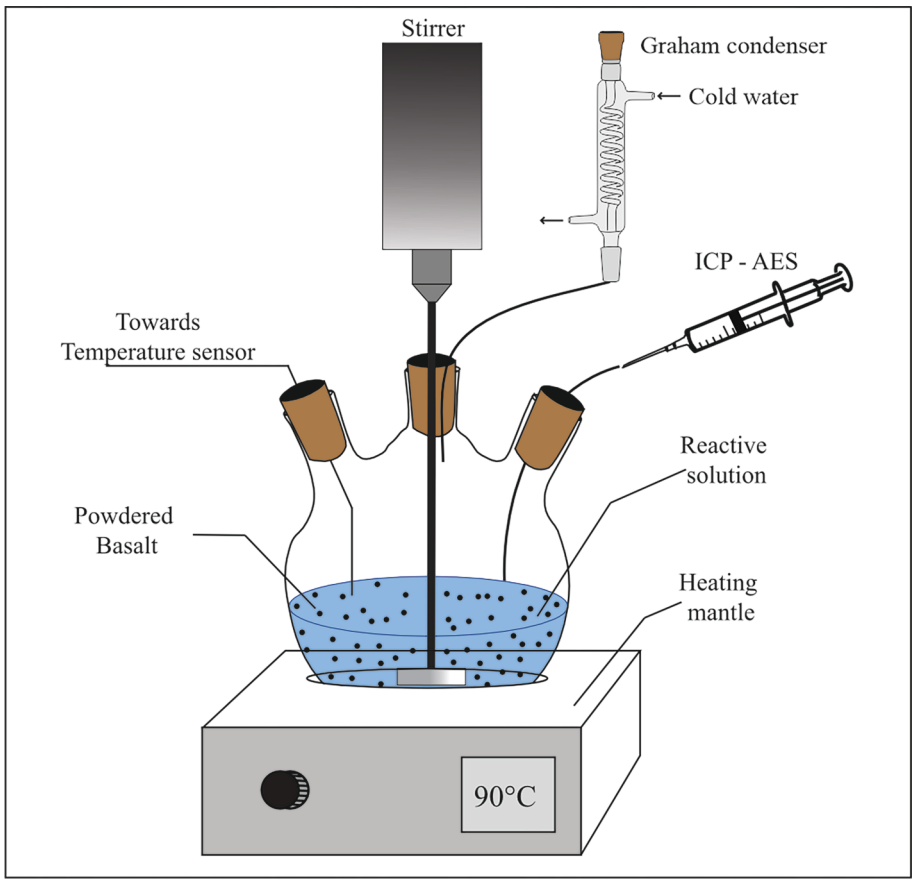

Fig. 1. Schematic diagram of reaction setup used to perform basalt water interaction.

using a 0.2 μm cellulose filter before analysis. After each sampling step, outlet systems were cleaned and dried to avoid contamination from the previous sample. The reaction was kept at 90 °C with a 1:500 rock-water ratio (0.6 g rock in 300 ml solution). Graham condenser was attached to flask with a sealed top to condense vapour and avoid increased pressure in the reaction chamber. The pH of the reacting solution was measured at regular intervals by inserting a pH-measuring electrode connected to a digital meter. pH measurement was calibrated for 90 °C. The starting fluid was slightly alkaline, with a pH of 8.3. Reacting alkaline fluid was prepared using NaOH (Merck) in milli-Q water.

2.3. Analytical Methods

The surface area of the grains was measured using Brunauer-Emmett-Teller Method (BET). The crystalline and amorphous nature of basalt glass and the secondary clay products was evaluated with X-ray diffraction (XRD). The crystal chemistry of raw glass and the secondary product was studied using Fourier transform infrared (FTIR) spectroscopy. Textural, morphological and analytical study of sub-micron-sized secondary product was performed under scanning electron microscopy (SEM) with energy dispersive X-ray spectroscopy (EDS). The chemical composition of fluid and basalt glass was determined using inductive coupled plasma atomic emission spectroscopy (ICP-AES) and mass spectroscopy (MS).

The specific surface area of the samples was measured on Quantachrome Nova 2000e at the University of Vienna, Austria, using the six-point Brunauer-Emmett-Teller (BET) method. The sample with grain size 36–56 μm has a surface area of 4.51 ± 0.01 $m^2g^{-1,}$ while sample with grain size < 36 μm has a surface area of 6.38 ± 0.33 $m^2.g^{-1}$. The X-ray diffraction (XRD) analysis was performed at the Department of Earth Sciences, Indian Institute of Technology (IIT) Bombay, with Empyrean Panalytical XRD. X-ray was generated with a Cu target. The X-ray spectra were collected with 0.01° step increment and a count time of 58.395 s per step using Cu Kα radiation transmitted through 0.04 rad soller slit opening and 1.52 mm anti-scatter slit. The diffracted beam was detected using a PIXcel^{3D} detector.

The Fourier transform infrared (FTIR) measurements were performed on Thermo Nicolet 6700 and Bruker Vertex 80 FTIR systems at the Department of Earth Sciences and Sophisticated Analytical Instrument Facility (SAIF), IIT Bombay. Sample powder was mixed with KBr (2 mg of sample and 200 mg of KBr), and a pressed disc was prepared. Spectra were collected in the range of 400–4000 cm^{-1} with a resolution of 2 cm^{-1}. The decomposition of OH-stretching bands into component peaks was done using fityk 1.3.1 software (Wojdyr, 2010). It uses the Levenberg-Marquardt method for curve fitting. Curve fitting parameters were accepted based on a weighted sum of squared residuals (WSSR) parameters and agreement between calculated and experimental profiles.

The solution's Na, K, Ca, Mg, Al, and Si concentrations were measured using Spectro Arcos Inductively coupled plasma atomic emission spectroscopy (ICP-AES) at SAIF, IIT Bombay. The instrument was calibrated for 0.1 ppm to 100 ppm using a multielement standard prepared by serial dilution. The precision and accuracy of the analysis were better than 5 %, and the blanks were negligible. Accuracy and precision were continuously monitored using standard as unknown. The detection limit of the instrument was 0.01 ppm. Lithium concentration in the basalt glass and reacting fluid was measured using ThermoIcap quadrupole Inductively coupled plasma mass spectroscopy (ICP-MS) at the Department of Earth Sciences, IIT Bombay. BHVO-2 (Hawaiian basalt), RGM-2 (Rhyolite from Glass Mountain), STM-2 (Syenite), SBC-1 (Brush Creek shale), and SCO-2 (Cody shale) rock standards were used for calibration and accuracy during the Li concentration measurement of

basalt glass. Rock standards and basalt glass were digested using microwave acid digestion technique. Reacting fluid chemical analysis was calibrated using multielement standards of different concentrations, prepared by serial dilution. Precision and accuracy in both analyses were below 5 %.

Imaging of submicron to sub-nano meter sized secondary product of basalt glass alteration reaction was done at Physical Research Laboratory (PRL) India, using a scanning electron microscope (SEM) (model JEOL IT300). Insitu compositional measurement was done under an energy dispersive spectrometer (EDS) attached to SEM. An ion sputtering coater was used to create a conductive carbon layer before imaging to avoid charging in SEM. In situ chemistry of basalt glass grains was measured at the Department of Earth Sciences, IIT Bombay (India), using a Cameca SX-50 electron microprobe analyser (EPMA) with five wavelength dispersive spectrometers. Glass grains were mounted in epoxy stubs and finely polished. Carbon coating was done before analysis under EPMA to avoid charging. Analysis was done using a pointed probe (diameter 2 μm) at an acceleration voltage of 15 kV and a fixed probe current of 20nA.

2.4. Geochemical Modelling

PHREEQC computer program (C++ language) was used to perform aqueous geochemical calculations at low temperatures (Parkhurst and Appelo 1999). Speciation and solubility geochemical modelling was done for each reaction step (sample) to calculate product minerals saturation indices (SI). The molar concentration of elements in each sampled solution, fluid temperature, pH, and volume were used as input parameters to calculate the activity of chemical species. The Graham condenser attached to the chamber maintained pressure at 1 atm in the reaction chamber. Hence, the modelling parameter for pressure was set by default as 1 atm. The simulated pH was also compared with the experimentally measured pH (see Table S4 and Table S5). The activity of chemical species was used to calculate the Gibbs free energy of each reaction step (ΔG_r). The Carbfix and MINTEQ databases were used in the modelling.

2.5. Dissolution rate determination

The kinetics of dissolution is a measure of rate of mass dissociation from reactant. Element concentration continuously increases during dissolution in a closed system, while an open system results in a mechanical steady state of elements defined by flow rate. The amount of element released in the solution at any stage of the reaction can measure the dissolved mass of basalt glass if the element does not fractionate in any secondary product. Many researchers have considered Li as a tracer element for dissolution studies (Vernaz et al., 2001; Techer et al., 2001; Curti et al., 2006; Gin et al., 2013; Parruzot et al., 2015). Li concentration and changed solution volume were used after fluid removal in the previous sampling step to calculate the mass loss of basalt during dissolution. Normalised mass loss (NML) measures mass loss per unit surface area of reacting basalt. It can be calculated using the following equation:

$$NormalisedMassLoss(NML) = ({}^{n}C_{Li} \times {}^{n}V)/(R_{Li} \times S) \quad (2)$$

$^{n}C_{Li}$ = concentration of Li in fluid at n^{th} hour
^{n}V = volume of fluid at n^{th} hour.
R_{Li} = concentration of Li in rock.
S = total surface area ($m^2 g^{-1}$).

The alteration rate of basalt glass for each sampling step can be measured using the difference between normalised mass loss in two consecutive steps and the time gap between them. The formula to measure alteration rate in "mole m^{-2} s^{-1}" can be written as follows:

$$Alterationrater_{[i+(i+1)]/2} = \left[(NML)^{i+1} - (NML)^{i}\right]/\left[\left(t^{i+1} - t^{i}\right) \times (molecularmass)\right] \quad (3)$$

2.6. Gibbs free energy calculation

In recent years, mineral dissolution kinetics has been investigated using transition state theory. Nagy et al. (1991), Nagy and Lasaga (1992), Lasaga et al. (1994) proposed a model to study kinetics by incorporating "reaction affinity" term in ΔG_r measurement ($A = -\Delta G_r$):

$$r = k^{+}\left(\prod_J a_J^{m_J} f(\Delta G_r)\right) \quad (4)$$

r is the mineral dissolution rate, k + is the rate constant, $\prod_J a_J^{m_J}$ shows the activity product of species in the solution, $f(\Delta G_r)$ is the Gibbs free energy function, which can be expressed as follows (Aagaard and Helgeson, 1982; Nagy et al., 1991; Lasaga et al., 1994):

$$f(\Delta G_r) = 1 - exp(n\Delta G_r/RT) \quad (5)$$

For the current experimental setup, we measured Gibbs free energy of each incremental reaction with dissolution of basalt glass using the following equation:-

$$Q/K_e = exp(\Delta G_r/RT) \quad (6)$$

Q is the ion activity product, K_e is the solubility product, R is the ideal gas constant, T is the temperature, and ΔG_r is the reaction Gibbs free energy. The final rate equation used was:

$$R = k^{+}(1 - Q/K_e) \quad (7)$$

Following Paul (1977), basalt glass solubility product (K_e) was calculated by considering glass a mixture of oxide. x_i (molar fraction) and K_i (solubility products) of each oxide are known. Hence, the solubility of glass has been calculated using ideal solid solution relation (Bourcier et al., 1992; Advocat et al., 1997; Leturcq et al., 1999):

$$\log Ke = \sum_i x^i \log K^i + \sum_i x^i \log x^i \quad (8)$$

3. Results

3.1. Basalt Glass Characterisation

The Hawaiian basalt glass powder X-ray diffraction (XRD) pattern has no discernible peaks, indicating the absence of crystalline phases. XRD spectra showed a broad low-intensity hump in the range of 25–30° 2 θ (Fig. 2A), characteristic of amorphous material (Dehouck et al., 2014; Rowe and Brewer, 2018;). The specific surface area (SSA) of basalt glass, in size range < 36 μm, is 6.38 ± 0.33 m^2/g; comparatively, 36–56 μm size fraction has a lower, 4.51 ± 0.01 m^2/g, specific surface area (measured using the BET method) (Table1). SEM images of basalt grains show several characteristic morphological features of amorphous glass, e.g., conchoidal fractures, blocky irregular surfaces, etc. (Loocks et al., 2010). Under an electron microscope, glass grains appear micro-pores or pits-free. BSE images (Fig. 2C) of glass fragments under EPMA show homogeneous grey shades across all grains, suggesting a lack of compositional heterogeneity within and between the grains. The bulk chemistry of basaltic glass measured with ICP-AES shows that almost all element's concentration lies within the 1σ range of 25 grains chemistry measured under EPMA (Table 2). This confirms the compositional homogeneity of basaltic glass fragments and discards the possibility of site-specific variation in the glass dissolution reaction due to chemical heterogeneity of the reacting substrate within a system. The total alkali in glass ($K_2O + Na_2O$ = 2.87 wt%) is less than 5 wt%, and SiO_2 (52.50 wt %) lies between 45 and 54 wt%, which is in the range of basalt as per the

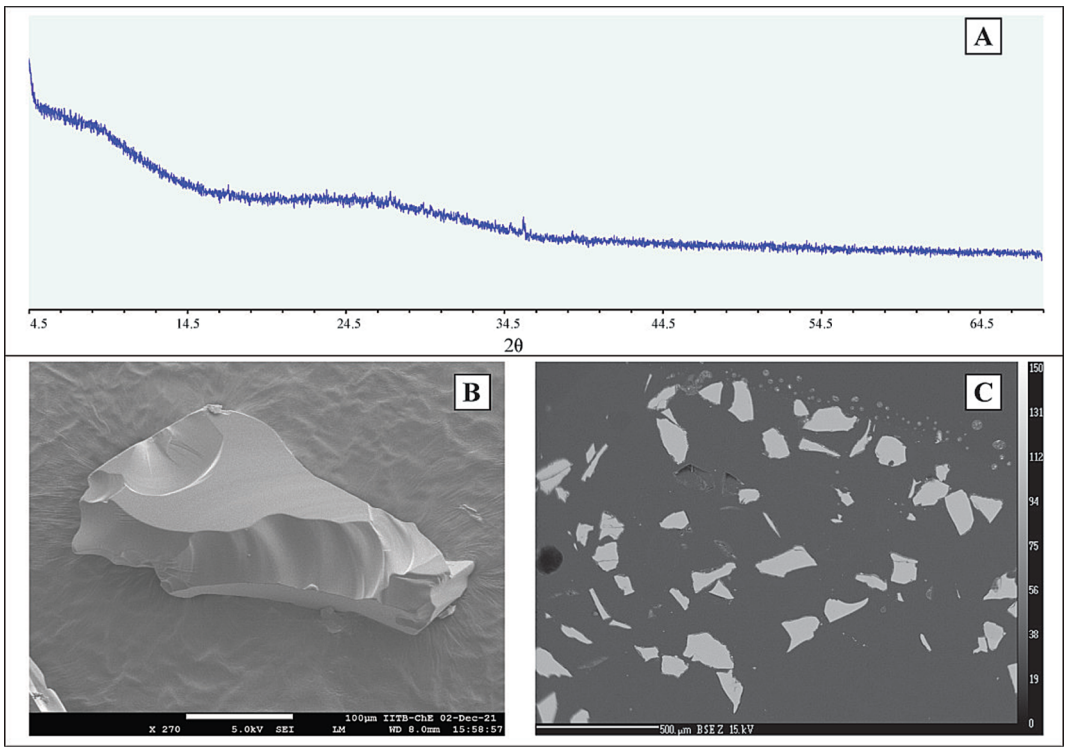

Fig. 2. Basalt glass characterisation. (A) X-ray diffractogram of the Hawaiian basalt glass used in the experiment. (B) Secondary electron (SE) image of basalt glass under scanning electron microscope (SEM) (scale bar in the image is 100 μm). (C) Backscattered electron (BSE) image of basalt glass grains under electron probe micro analyser (EPMA) (scale bar is 500 μm).

Table 1
Experimental setup.

Setup no.	Rock: water ratio	temperature	Grain size	Surface area
1	1:100	90 °C	36–56 μm	4.51 ± 0.01 m^2/g
2	1:100	90 °C	<36 μm	6.38 ± 0.33 m^2/g

Table 2
Glass composition.

Element/ Oxide	EPMA of 25 grains (Anhydrous basis)		ICP AES (Anhydrous basis)	ICP-MS
	Average (%)	dev	Bulk chemistry (%)	(ppm)
Na_2O	2.46	0.043	2.25	–
MgO	6.47	0.082	7.56	–
Al_2O_3	13.6	0.068	12.6	–
SiO_2	51.9	0.466	50.57	–
P_2O_5	0.25	0.026	0.22	–
K_2O	0.37	0.025	0.36	–
CaO	9.92	0.133	11.47	–
TiO_2	2.25	0.068	2.5	–
MnO	0.17	0.027	0.17	–
Fe_2O_3	12.5	0.17	12.32	–
Li	–	–	–	5.27

TAS diagram of rock classification (Bas et al., 1986). FeO (t), MgO, Al_2O_3, TiO_2, and CaO also lies in the range of basalt. Li concentration in the basalt glass is 5.27 ppm (Table 2).

3.2. Evolution of pH and elements in fluid

The experiment started with slightly alkaline fluid (pH = 8.7) under a closed system. Unlike previous studies in open systems (far from equilibrium), closed systems show a dynamic evolution in the fluid composition (Crovisier, 1987, 1988a, 1988b; Daux, 1997; Techer et al., 2001; Oelker and Gislason 2001; Gislason and Oelker, 2003; Wolff-Boenisch, 2004; Declercq et al., 2013). The pH increases rapidly and reaches a plateau at 9.35–9.40 within 48 h of the reaction. After 284 h, pH drops to an initial value of ~ 8.5 and remains almost constant from 300 h onwards (Table 3). Lithium (Li) concentration in the basalt glass is in trace amount (~5 ppm). As Li is highly mobile, it liberates from reacting solid quickly and does not fractionate to any secondary phase. The concentration of Li in both dissolution experiments shows an overall trend of increase with time (Table 3), reaching a value of 4 ppb in 548 h.

The Fe concentration was below the detection limit of analysis. This experimental setup has oxidation conditions similar to recent earth's surface. Under oxidising conditions, iron attains a ferric state (Fe^{+3}) and goes into solid phases, e.g., iron (oxy) hydroxide, resulting in very low Fe^{+3} (aq) (Fox, 1988). Other than Fe, all major cations present in basalt (Na, K, Ca, Si, Mg and Al) have been measured in reacting fluid to monitor the dissolution reaction and subsequent fluid evolution in both experiments. Na, K increases rapidly compared to Ca, Mg, Al and Si in the first few hours under both experimental setups (Fig. 3). Except for Mg, other cations (Na, K, Ca, Al and Si) reach their local maximum concentration after 54 h, followed by a sudden decrease within 6 h (Fig. 3). After 60 h, cations (Na, K, Ca, Al and Si) concentration in solution continuously increases with different trends. The elemental concentration evolution of Mg behaves differently. Mg reaches a plateau value of ~ 1.70 ppm at 20 h and remains almost the same till 54 h. This is followed by a continuous drop in concentration, which is contemporary to other cations' concentration drop stage until Mg concentration exceeds the detection limit. The time of Mg disappearance from the solution differs in both experiments, 164 h in < 36 μm and 236 h in 36–56 μm. Cations show a change in the concentration increment behaviour from the Mg loss point in the solution. This concentration evolution pattern is similar in both experimental conditions.

Table 3
Elemental Composition evolution in both experimental setup (<36 μm and 36–56 μm).

time (h)	pH	Reaction setup with < 36 μm grain size								Reaction setup with 36–56 μm grain size							
		concentrations							Normalised mass loss (g/m^2)	concentrations							Normalised mass loss (g/m^2)
		Si (ppm)	Al (ppm)	Na (ppm)	Ca (ppm)	K (ppm)	Mg (ppm)	Li (ppb)		Si (ppm)	Al (ppm)	Na (ppm)	Ca (ppm)	K (ppm)	Mg (ppm)	Li (ppb)	
2	8.7	7.11	0.77	11.32	1.13	0.89	0.73	1.34	–	1.31	0.38	15.14	0.5	29.04	0.09	0.94	19.79
4		9.02	0.88	7.28	1.77	0.79	1.12	0.51	7.56	2.35	0.36	6.43	0.95	11.66	0.35	0.44	9.22
6		10.02	0.49	8.56	2.19	0.85	1.29	3.33	–	4.41	0.37	6.79	1.29	11.59	0.41	0.82	17.12
8		10.87	0.73	6.51	2.39	0.78	1.33	0.71	10.43	6.11	0.33	7.11	1.51	12.15	0.71	1.46	30.35
10		14.54	0.95	24.37	0.37	0.64	bdl	0.84	12.29	7.24	0.49	6.93	1.69	11.96	0.83	0.39	8.07
12		11.28	0.51	7.27	2.51	0.74	1.38	2.96	–	8.49	0.64	7.4	1.79	12.13	0.96	1.67	34.43
14		12.29	1.61	6.72	2.73	0.92	1.36	0.55	7.98	9.29	0.68	7.02	2.37	11.78	1.11	0.47	9.65
16		12.7	1.48	6.12	2.89	0.66	1.43	0.46	6.65	9.3	0.5	7.03	2.13	11.96	1.06	0.59	12.06
18	9	13.67	2.13	6.1	3.21	1.49	1.53	0.61	8.78	13.32	1.98	6.12	3.15	1.54	1.44	0.66	13.43
20		17.23	1.4	11.42	5.98	3.7	1.75	0.5	7.16	14.25	1.34	13.76	5.33	27.83	1.67	0.8	16.21
22		20.01	1.31	11.56	6.28	3.53	1.77	0.59	8.41	17.09	1.56	13.69	5.1	27.67	1.71	0.6	12.11
24		23.13	2.21	11.65	6.47	3.43	1.68	0.61	8.66	21.98	1.9	14.11	5.59	28.39	1.69	0.73	14.66
28		24.18	1.57	13.62	7.16	4.73	1.69	0.78	11.03	21.71	1.68	12.97	6.26	26.4	1.7	0.86	17.2
32		23.13	1.72	13.83	6.85	27.65	1.91	0.65	9.15	23.4	2.1	12.12	7.28	3.45	1.68	0.89	17.72
36		25.77	2.02	12.27	7.3	3.73	1.62	0.77	10.79	25.16	1.33	16.26	6.47	31.09	1.79	1.44	28.55
40		28.82	2.08	12.4	7.1	3.78	1.59	0.83	11.58	27.51	2	14.76	6.08	29.33	1.71	0.61	12.04
44		32.36	2.07	12.86	7.75	4.01	1.52	0.75	10.42	28.3	1.57	14.23	6.64	28.57	1.69	0.81	15.92
48	9.3	32.4	1.5	13.76	8.09	4.2	1.46	0.98	13.55	31.96	2.68	14.85	7.32	29.34	1.83	1.19	23.28
54		33.59	2.91	13.47	8.83	4.39	1.38	1.69	23.26	28.99	2.79	15.44	8.3	32.34	1.95	1.14	22.2
60		16.42	1.61	7.62	3.84	2.26	0.94	1.26	17.27	15.71	1.44	8.96	3.33	19.31	1.4	0.78	15.12
66		17.33	1.13	7.95	4.07	2.12	0.83	1.2	16.37	14.78	1.31	9.1	3.13	19.07	1.24	0.82	15.82
72		16.94	1.25	7.59	4.12	2.34	0.67	1.44	19.56	16.8	1.39	9.31	3.48	19.74	1.12	1.93	37.08
78	9.37	18.55	1.25	8.17	4.54	8.6	0.68	1.38	18.65	16.89	1.4	9.05	3.64	20.49	1.07	1.78	34.04
84		18.73	1.3	8.22	4.5	8.65	0.69	1.89	25.43	17.71	1.57	10.05	3.97	21.66	1.11	1.26	23.98
90		19.42	1.16	8.61	4.37	9.03	0.48	1.8	24.11	17.94	1.88	9.81	3.55	21.42	0.84	1.57	29.75
96		20.09	1.25	8.47	4.59	8.81	0.45	1.28	17.06	18.76	1.57	10.39	3.82	22.62	0.92	1.58	29.8
102		31.52	1.01	10.07	5.77	9.94	0.48	1.43	18.98	26.49	1.3	10.82	4.47	24.44	0.87	1.57	29.47
108		27.71	1.01	9.63	5.39	9.41	0.39	1.65	21.79	24.22	1.14	10.86	4.4	23.9	0.7	1.42	26.53
114		27.1	1.55	9.3	5.57	9.3	0.24	–	–	21.32	0.93	10.53	3.84	22.68	0.56	1.48	27.52
120		25.42	0.95	9.9	5.33	9.71	0.28	1.31	17.14	21.55	0.91	10.75	4.4	22.99	0.51	1.8	33.32
126	9.3	23.78	0.85	9.43	5.33	12.04	0.17	1.88	24.48	20.94	1.18	9.89	4.1	22.17	0.44	1.6	29.47
132		25.04	1.05	9.62	5.26	12.32	0.17	1.38	17.88	26.1	0.97	12.25	4.6	26.85	0.52	1.34	24.57
138		25.55	1.01	10.73	6.32	13.59	0.33	1.42	18.32	22.93	0.93	11.76	4.6	25.43	0.55	1.33	24.27
144		26.06	1.3	10.3	5.72	13.44	0.07	1.57	20.15	22.32	0.94	11.93	4.48	25.68	0.47	2.16	39.22
150		24.49	1.05	10.27	5.32	12.93	0.02	1.62	20.69	21.61	1.19	11.01	4.16	23.89	0.33	1.28	23.13
164		26.24	0.91	11.24	5.58	13.84	bdl	1.81	23.01	22.13	0.86	11.28	4.1	24.19	0.14	1.45	26.07
188	9.35	25.83	0.58	11.38	5.19	13.74	bdl	1.99	25.17	23.01	0.75	12.23	4.59	25.71	0.26	2.35	42.05
212	9.35	28.31	0.81	11.88	5.87	14.21	bdl	2.18	27.44	23.75	0.8	12.28	4.37	25.6	0.1	2.12	37.75
236		30.67	0.96	12.48	5.58	15.17	bdl	2.1	26.30	27.95	1.42	13.03	4.63	26.81	bdl	2.72	48.2
260		33.15	1.21	12.73	6.27	15.51	bdl	1.95	24.30	30.15	0.64	14.5	4.58	29.2	bdl	2.07	36.5
284	9.41	35.08	0.45	14.14	5.84	16.54	bdl	2.31	28.65	28.43	0.37	14.7	4.38	31.01	bdl	2.26	39.65
308		36.92	0.4	14.85	5.85	17.37	bdl	2.45	30.23	36.94	1.02	17.17	2.66	32.77	bdl	2.14	37.36
332	8.85	37.3	0.61	16.08	2.16	16.82	bdl	2.2	27.01	37.1	0.97	17.98	1.88	34.23	bdl	1.7	29.53
356		38.3	0.71	14.35	2.73	16.31	bdl	2.1	25.65	38.79	0.98	17.09	3.2	36.72	bdl	2.97	51.32
404	8.85	43.56	0.6	17.19	3.27	18.35	bdl	3.86	–	41.43	0.69	19.15	2.71	37.28	bdl	7.45	–
452	8.85	50.05	0.56	19.93	4.55	19.89	bdl	–		46.93	0.6	21.54	2.16	41.39	bdl	3.15	53.88
548	8.6	59.07	0.46	22.69	8.74	23.08	bdl	4.03	–	54.73	0.47	23.17	6.63	45.97	bdl	3.92	66.71

bdl = below detection limit

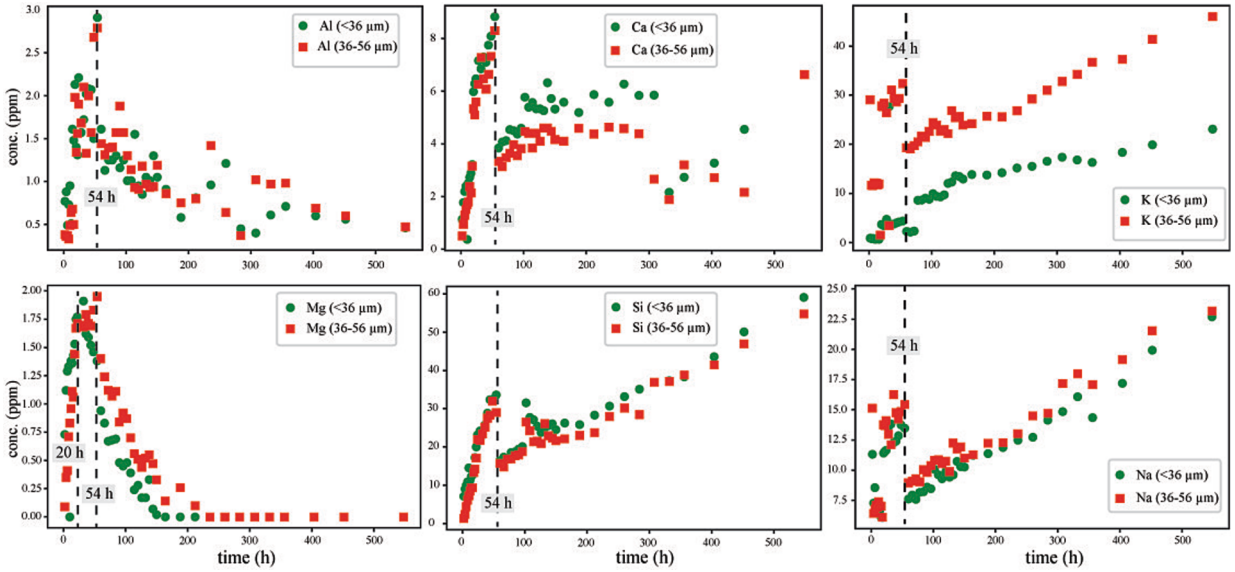

Fig. 3. Evolution of element concentration in reacting fluid, with time. Each block in the diagram represents one element mentioned in the box. The green circle indicates the reaction setup with < 36 μm and the red box indicates the reaction setup with 36–56 μm basalt glass fraction.

3.3. Secondary products

Pre-experimental characterisation of glass surfaces has been performed in detail. Submicron features have been investigated under an analytical electron microscope (SEM-EDS). SEM imaging of basalt glass surface in both experiments shows secondary products in the form of coating. The morphologies of secondary products can be categorised into two major types: a) honeycomb-like structure grown on the glass surface (Fig. 4 A, C) and b) equant and/or ellipsoid grains accumulated on the surface (Fig. 4 B, D). In both experiment setups, these features are present with varying chemical compositions and assemblages, encompassing the signature of reaction progress associated with their formation (Table 4).

In the experiment with < 36 μm glass fraction, a secondary product having honeycomb morphology is a dominant phase with a size of up to a few microns (Fig. 4 A). In Fig. 4A, the sporadic presence of small particles with honeycomb structures attached to the large grain surface indicates a smaller fraction of the original basalt glass. Chemically, both features have similar compositions and are slightly modified to the initial basalt glass (Table 4). Cation ratios, Si/(Al + Mg + Fe) and Al/Si, based on 11 oxygen, lie between 1–2 and 0–0.4, respectively, depicting a close chemical affinity towards nontronite or saponite type of 2:1 phyllosilicate (Fig. 4 E) (Cuadros et al., 2013). Other secondary products in this experiment setup are aggregates of phases with ellipsoidal morphology and equant granular morphology (Fig. 4B). Chemically, ellipsoid phases have Si/(Al + Mg + Fe) between 1–2 and Al/Si > 0.4, which can be compositionally categorised as montmorillonite (2:1 phyllosilicate) (Fig. 4E). Ellipsoid phases are Mg depleted and K enriched compared to honeycomb morphology (Table-4). Equant granular phases, co-existing with ellipsoidal morphotypes (Fig. 4B), are smaller in size (<0.5 μm) with relatively lower Fe, Mg and Ti with increased anions (oxygen) wt%, suggesting calcium-aluminium hydrous silicates (CAHS). The cation ratios, 2 < Si/(Al + Mg + Fe) < 1 and Al/Si > 1, fall out of the 2:1 phyllosilicate range (Fig. 4E).

In the experiment with 36–56 μm glass grains, secondary products having honeycomb morphology are dominant phases grown as glass

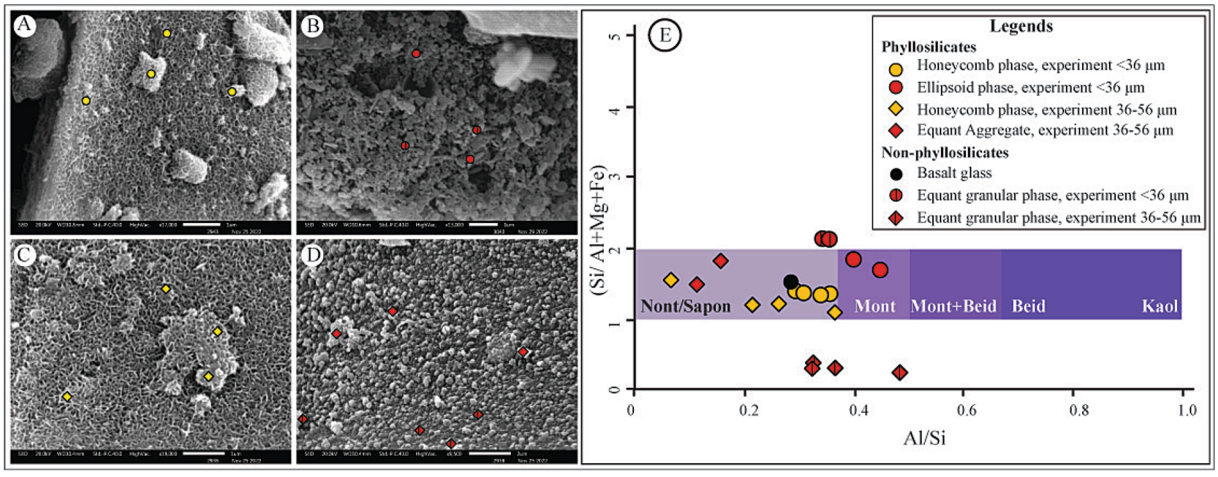

Fig. 4. Analytical electron microscopic (SEM-EDS) investigation of secondary products formed in both experiments, (A), (B) are products in < 36 μm experiment while (C), (D) indicate 36–56 μm experiment. Circular and diamond shapes indicate the spots for analytical measurement in < 36 μm and 36–56 μm experiments, respectively. Plain circles and diamonds indicate the features with phyllosilicate equivalent chemistry. Circles and diamonds with vertical bars indicate features with non-phyllosilicate chemical signatures. (A) Honeycomb morphology of secondary product grown as coating of basalt glass surface (B) Aggregate of ellipsoid and equant granular phases. (C) Honeycomb morphology of secondary product. (D) Equant aggregate and equant granular-shaped secondary product.

Table 4
Chemical composition of secondary products formed in both set up of experiments.

Element	Secondary products in < 36 μm grains experiment						Secondary product in 36–56 μm grains experiment					
Wt %	Honey comb shape			Ellipsoid shape		Equant phase	Honey comb shape			Equant aggregate	Equant phase	
Si	23.49	23.05	25.49	23.8	25.82	24.13	26.02	24.05	25.56	24.68	21.95	26.23	27.17	10.47	6.84	8.98	6.55	11.19
Al	8.02	7.49	7.16	7.02	10.23	9.88	7.92	8.85	6.06	8.95	1.55	4.51	2.84	4.08	3.27	3.18	2.78	2.3	2.63	2.42
Na	1.46	1.74	1.82	1.87	0.4	0	0.52	1.16	0.45	0.09	0.69	0.97	0.47	1.45	0.41	1.74	0.01	2.63	0	
Mg	4.46	4.3	4.16	4.87	1.43	1.13	0.56	1.78	3.88	3.4	3.01	3.81	0.6	2.55	1.46	0.39	1.92	0.27	0	
K	0.35	0.28	0.37	0.62	1.25	1.07	0.44	0.6	0.83	0	0.88	0.47	0.92	0.82	1.16	0	0	0.49	0.25	
Ca	6.8	6.36	7.73	6.24	6.66	5.5	6.96	5.31	9.62	13.25	13.85	11.22	4.72	7.49	7.93	10.12	9.13	10.47	12	
Fe	7.66	8.87	11.95	8.93	3.55	4.85	4.85	1.99	17.94	20.24	21.54	18.31	27.85	15.46	44.19	48.18	48.58	36.28	42.71	
Mn	0.74	0.34	0	0	0.48	0	0	0	1.22	0.15	0	1.29	0	0.75	0	1.53	0	1.62	1.6	
O	45.57	46.02	39.43	44.99	51.45	51.74	54.6	54.13	31.96	24.14	21.95	30.71	36.2	37	27.65	24.81	25.71	35.61	25.6	
Ti	1.44	1.55	1.89	1.66	0.72	0	0	0.15	3.6	4.21	3.24	2.41	0.17	3.24	3.46	3.22	2.88	3.78	4.24	

surface coating. Chemically, these phases are Fe (>17 wt%), Mg (>3 wt %) and Ca (> 9 wt%) enriched, with Si/Al + Mg + Fe (between 1–2) and Al/Si (< 0.4) values showing close affinity to nontronite/saponite, 2:1 phyllosilicate (Fig. 4E). Other secondary products are sub-nano-meter phases with equant growth. Based on their morphology, they could be categorised into two major types: (1) Equant aggregate phase and (2) Equant granular phase (Fig. 4D). Although equant aggregate phases show a compositional similarity with nontronite and saponite (Fig. 4E) because Si/(Al + Mg + Fe) lies between 1–2 and Al/Si < 0.4, but Mg (<3 %) is lower than honeycomb-shaped phases (Table-4). Equant granular phases are found at glass surfaces as isolated nano to micron-size mounds. They do not show chemical affinity towards any 2:1 phyllosilicate, Si/(Al + Mg + Fe), and Al/Si lies out of the range for phyllosilicate (Fig. 4E). High Fe (average 43 wt%, n = 5), Ti and low Mg, Si are distinct compositional identities of equant granular phases.

4. Discussion

4.1. Dissolution behaviour and kinetics

Dissolution reaction under an open system attains a steady state far from equilibrium, resulting in no precipitation. Hence, mobile cations, e.g. Na and K, were used as a proxy to measure the extent of dissolution in open systems (Daux et al., 1997; Techer et al., 2001). Closed systems reach equilibrium due to a continuous increase in the elemental concentration, resulting in the precipitation of saturated phases and causing the fractionation of elements in the solid against the release in the solution. After an extent of reaction progress, closed systems experience a combination of dissolution and precipitation, requiring a highly mobile element (Li) as a proxy to calculate the dissolution extent, behaviour and kinetics. Although Li is highly mobile, it can substitute Mg in the octahedral clay sites due to similarity in ionic radii (Shannon, 1976). Li fractionation in the current experimental condition, calculated based on expression of partition coefficient ($\log D_{Li}$) proposed by Decarreau et al. (2012), is within the error of Li concentration measurement for quadrupole (Q)-ICPMS (see Table S9 and Table S10). Note that this calculation is based on expression proposed for hectorite (Li-Mg clay). The current experimental product's Mg concentration (~4%) is lower, leading to a lower partition coefficient.

The Li concentration measured at each step of dissolution reaction gives the extent to which basalt glass was dissolved (using eqn (1). Both size fractions of basalt glass show a similar trend of normalised mass loss variation during the entire extent of dissolution reaction (Fig. 6). Smaller fraction (<36 μm) has higher values of normalised mass loss in comparison to larger fractions (36–56 μm) at any extent of time (Fig. 6), due to larger surface area (Table-1). Starting at 100 h, normalised mass loss increases rapidly for both the fraction and slows down afterwards. Mass loss evolution with time is exponential ($r^2 = 0.74$–0.77) (Fig. 6). Basalt glass dissolution rate for a smaller fraction (<36 μm), calculated in the initial days of reaction, is (r_0) 1.7×10^{-9} mol.m^{-2}.s^{-1}, which lowers by 100 times by the end of 24 days to (r) 5.7×10^{-11} mol.m^{-2}.s^{-1}. The initial dissolution rate of a larger fraction is 2.5×10^{-9} mol.m^{-2}.s^{-1}and the final rate (after 24 days) is 6.5×10^{-11} mol.m^{-2}.s^{-1}.

In both experimental setups, elemental evolution patterns with time are similar (Fig. 3). Elemental ratios (Li/Si, Al/Si, Mg/Si, Ca/Si) in reacting fluid show higher values in the initial 20 h (Fig. 5) for basalt glass, suggesting a preferential removal of modifier cations in silicate structure due to proton-metal exchange reaction (Ghiara et al., 1993, Gin et al., 2013). Such dissolution behaviour indicates an incongruent nature. The protonation of silicate structure causes an increase in pH (Fig. S3). The ratio of Li/Si in fluid and basalt glass reaches similar values after 20 h (Fig. 5). It remains almost constant later, indicating the congruent nature of the dissolution reaction afterwards, with minor fluctuations signifying the equilibrium with saturated phases. Other cations (Al, Mg, Ca) ratio with Si in the fluid decreases below the glass values (Fig. 5). It reaches a plateau, indicating preferential

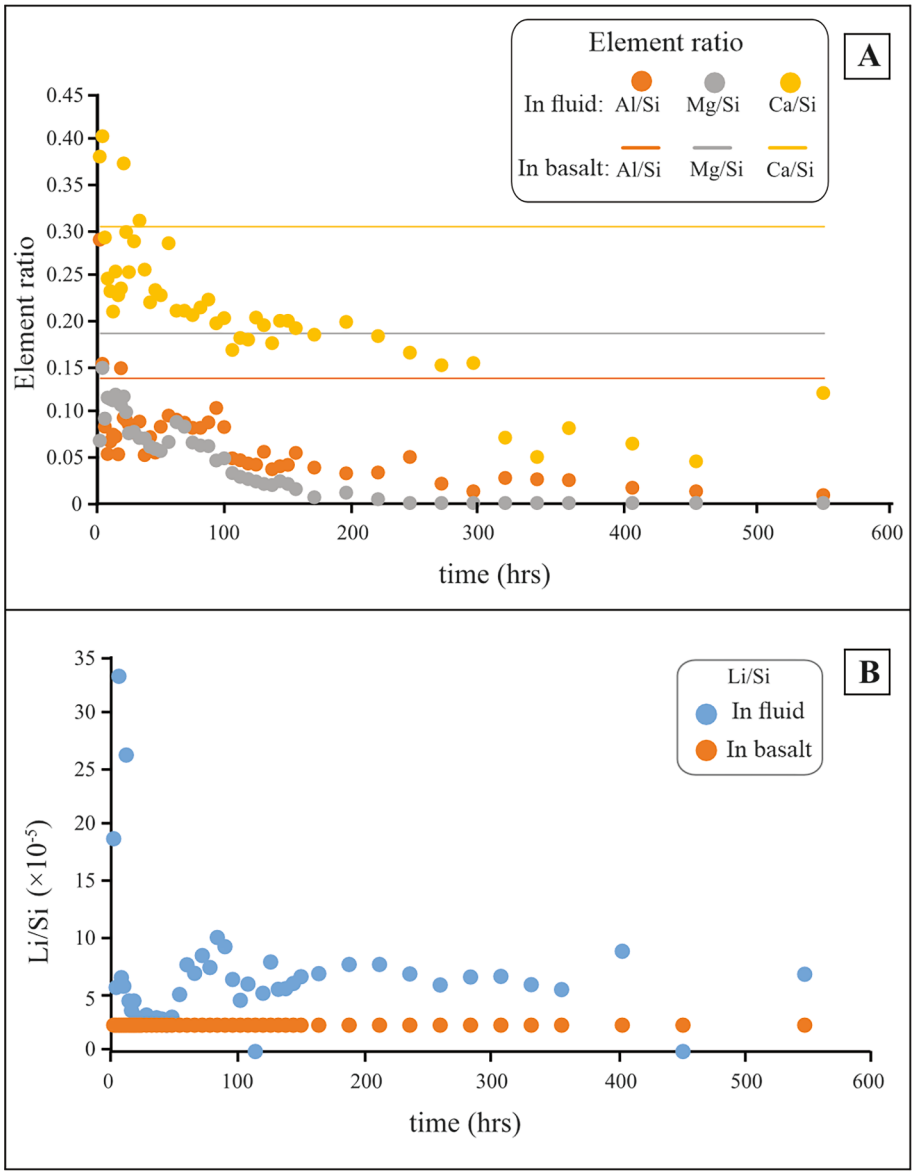

Fig. 5. Evolution of elemental ratios with time, showing congruency and incongruency stages during dissolution. (A) Variation of Al, Mg, and Ca ratio with respect to Si during the entire extent of reaction. Circular dots indicate elemental ratio in fluid, and lines indicate ratio in basalt rock. The colours of the symbols are specific to the elements. (B) Li and Si ratio evolution with time. The blue dot indicates the ratio in reacting solution, while the orange dot indicates the constant value in basalt glass.

incorporation of these cations in the precipitation of secondary phases.

4.2. Secondary product formation mechanism: Implication towards phyllosilicate nucleation

Basalt glass dissolution reaction in a closed system has resulted in a continuously evolving fluid chemistry (Fig. 3). Aqueous geochemical modelling of this dynamic system shows the possible mineral phases undergoing supersaturation (see Table S1 for saturation index) at each stage of reaction progress (Fig. 7). Despite the continuous dissolution of glass, Mg concentration in the reacting solution reached a plateau within 20 h, corresponding with brucite [$Mg(OH)_2$] supersaturation (Fig. 7). Although brucite was an oversaturated phase from the 4th hour onwards, according to thermodynamics, its precipitation started with a lag of 14—16 h due to nucleation delay associated with lower degree of supersaturation, called induction period (Spanos and Koutsoukos, 1998; Brown, 2011). At 54th hour, a decrease of elemental concentration, e.g. Al, Si, Ca along with Mg in the reacting solution signifies the start of another solid phase, Ca-montmorillonite (smectite), indicating oversaturation (Fig. 7) at this stage of the system. After 6 h of brucite and smectite coprecipitation, Mg concentration reaches below ~ 1 ppm, resulting in a brucite undersaturation state at 60th hour, leaving smectite (Ca- montmorillonite) as the only saturated phase afterwards. The sudden disappearance of montmorillonite (smectite) from an oversaturation state at the 160th hour corresponds to Mg concentration below the detection limit (0.01 ppm). Record of element concentration evolution and theoretical estimation of mineral supersaturation suggested two significant stages of smectite precipitation in this system: (1) smectite (2:1 phyllosilicate) coprecipitation with brucite and (2) only smectite precipitation.

SEM-EDS study of secondary products shows honeycomb-shaped features in both experimental conditions with high Mg (>3 wt%). Many researchers have reported the honeycomb-shaped morphology as a characteristic feature of smectite (Keller et al., 1986; Fiore et al., 2000; De La Fuente et al., 2000; Christidis, 2006). Compositionally, the honeycomb structure is closely related to the nontronite and saponite

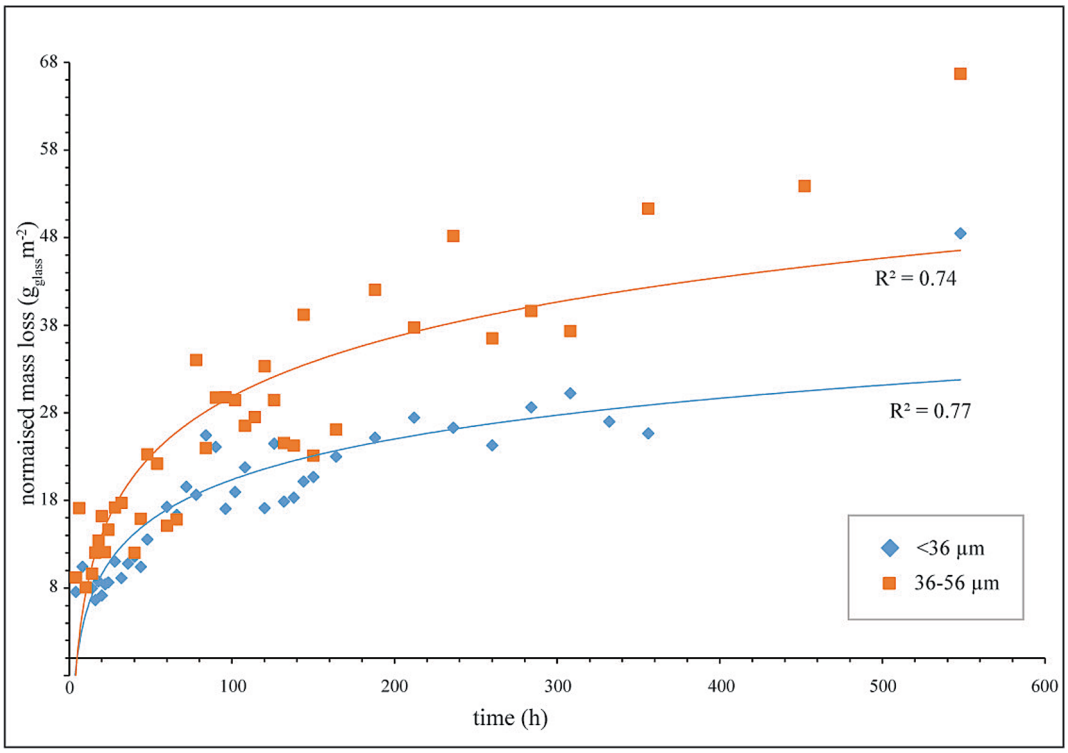

Fig. 6. Normalised mass loss plot to time. The blue diamond indicates the experiment with < 36 µm fraction of basalt glass. The orange square indicates an experiment with a 36–56 µm fraction of basalt glass.

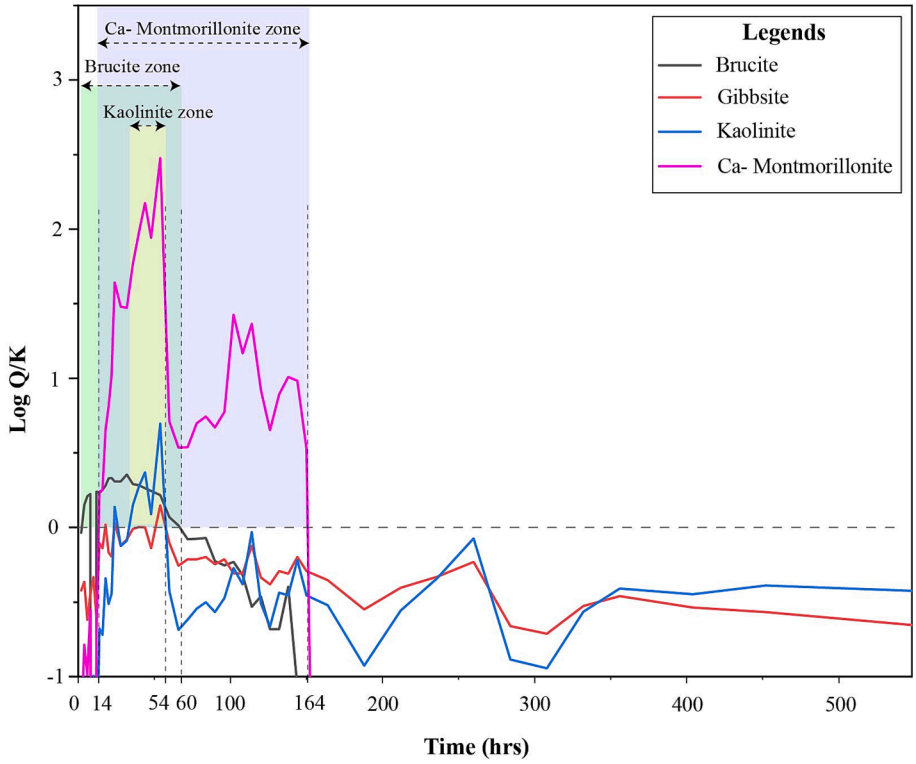

Fig. 7. Saturation index versus time for reaction setup with grain size (36–56 µm). Solid lines show minerals that reach the oversaturation state during the reaction; the colours are specific to the mineral variety. Coloured bands in the background of the image mark the zone of oversaturation of the specific mineral mentioned within the coloured band.

smectite (Fig. 4E). Other secondary products with smectite chemical affinity, e.g., the ellipsoidal and equant aggregate phases, have low Mg and high Fe. None of the secondary phases observed has brucite chemistry (Fig. 4), although fluid composition and thermodynamic modelling have shown a strong signature of precipitation (Fig. 3,7). This suggests either the transformation/incorporation of brucite structure into other stable phases or its dissolution, which should have shown an increased Mg concentration. After the first appearance of brucite in the system, there was no signature of Mg concentration increment, neglecting the dissolution hypothesis for the absence of brucite. Several studies have shown that brucite-like structure is an intermediate stage of smectite formation or transformation (Banfield et al., 1991; Bettison-Varga and Mackinnon, 1997; Meunier et al., 2010; Meng et al., 2018) since brucite has structural similarity with octahedral sheet of clay (Tsipursky and Drits, 1984; Chakoumakos et al., 1997). Hence, brucite constitutes the perfect template for smectite epitaxial growth. Brucite oversaturation before montmorillonite (smectite) saturation (Fig. 7) might facilitate high Mg smectite growth viz. honeycomb shaped in both experimental conditions (Table-4). The smectite oversaturation without brucite (Fig. 7) might indicate the secondary product formation stage with low Mg, e.g. ellipsoid phase and equant aggregate (Fig. 4E). Powder x-ray diffractogram collected at the end of the experiment shows an absence of diffraction peaks (Fig. S1), suggesting secondary products as amorphous precursors for crystalline mineral varieties. The FTIR spectra of both the experimental products in the stretching region of OH vibration show metal-OH bonds overlayed by glass spectra (Fig. S2). The experimental criteria for good crystallinity of the secondary product have been investigated through a separate experiment at elevated temperature and time, which will be part of another paper.

Equant granular phases of non-phyllosilicate chemistry (Fig. 4E), in both experimental setups, have low Mg and high Fe (Table 4). Such features are observed at the advanced stage of reaction progress after the expanse of Mg from the solution. Crovisier et al. (1992) performed thermodynamics calculations for basalt alteration in a closed system. They showed that the advanced state of smectite formation ($[SiO_2/MgO]_{glass}$ / $[SiO2/MgO]_{secondary\ product}$ = 1) is coupled with Ca-Al phases.

4.3. Chemical affinity and kinetics evolution with coupled dissolution-precipitation reaction

Numerous studies have been performed to propose appropriate models of minerals and glass dissolution (Daux et al., 1997; Techner et al., 1998; Techer et al., 2001; Hermanska et al., 2023). An accurate model to describe kinetics of dissolution requires intrinsic thermodynamic properties of mineral/rock, which depends on composition and internal structure, making any model challenging to fit for glass dissolution study as degree of polymerisation (internal structure) is specific to each glass. Although Hermanska et al. (2023) proposed a kinetic model for dissolution rate estimation of basalt glass in open systems, which are from equilibrium, a closed system still requires deeper insights. As closed system evolves, the cations released from dissolution reach equilibrium and start fractionating into solid, resulting in a quasi-steady state for certain cations. Alekseyev et al. (1997); Zhu et al. (2009) and Zhu et al. (2010) explained the change in the dissolution rate (r-ΔG_r relationship) of feldspar in closed system by coupled dissolution and precipitation. A dissolution reaction starts as far from equilibrium system and may reach to equilibrium. According to the transition state theory, as dissolution reaction progresses towards equilibrium, the rate decreases (r), and ΔG_r approaches zero. However, this theoretical trend has not been experimentally observed by Techer et al. (2001) for basalt glass dissolution in a closed system. We measured ΔG_r for each reaction step and correlated it with the dissolution rate.

The reaction of basalt dissolution in alkaline conditions can be written as:

$$(Si_1Al_{0.29}Ti_{0.04}Fe_{0.17}Mg_{0.22}Ca_{0.24}Na_{0.09}K_{0.01}O_{3.24}) + 2.12H_2O + 1.12H^+ + 0.28e^- \rightarrow H_4SiO_4^0 + 0.29Al(OH)_4^- + 0.09Na^+ + 0.24Ca^{+2} + 0.01\ K^+ + 0.17Fe^{+3} + 0.04Ti(OH)_5^- \quad (9)$$

The ion activity at each sampling step was calculated using PHREEQC. The ΔG_r of each reaction step has been calculated following Techer et al. (2001) (see Appendix A Supplementary material, Section S3, Chemical Affinity Calculation, Tables S2 – S8). The dissolution rate and ΔG_r relation is similar (Fig. 8) to Techer et al. (2001) observation.

The speciation and solubility modelling for each reaction step (Fig. 7) shows that brucite remains in equilibrium from the beginning of the reaction. Based on the elemental evolution study in the current experiment (Fig. 3), brucite can be considered a solid that precipitates from the beginning and remains saturated or incorporated for a more extended reaction period. We modified the total reaction affinity calculation by keeping the brucite, basalt, and reacting solution in equilibrium (see Appendix A Supplementary material, Section S3, Chemical Affinity Calculation). The ΔG_r at the advanced stage of reaction reaches a value of −37.4 kcal/mole (36–56 μm) and −34.8 kcal/mol (<36 μm). The ΔG_r for brucite precipitation is 33.8 kcal/mole, and the total Gibbs free energy of the system (total reaction affinity) reaches 0.8–3 kcal/mol. This suggests that incorporating thermodynamical parameters for precipitating phases explains the earlier shift of chemical affinity curve with rate, in accordance with TST. Hence, fit refinement can be done by incorporating the thermodynamic parameters of amorphous phases (Fig. 8). The complete reaction, which can explain the basalt and water interaction energetics and kinetics according to TST in a closed system can be expressed as a coupled dissolution and dissolution reaction:

$$(Si_1Al_{0.29}Ti_{0.04}Fe_{0.17}Mg_{0.22}Ca_{0.24}Na_{0.09}K_{0.01}O_{3.24}) + 2.12H_2O + 1.12H^+ + 0.28e^- \rightarrow H_4SiO_4^0 + 0.29Al(OH)_4^- + 0.09Na^+ + 0.24Ca^{+2} + 0.01\ K^+ + 0.17Fe^{+3} + 0.04Ti(OH)_5^- + \text{brucite} \quad (10)$$

4.4. Comparison between open and closed system kinetics and limitations of extrapolation

Numerous studies have investigated the kinetics of open systems, which are far from equilibrium. Daux et al. (1997) showed that open systems reach equilibrium with decrease in the flow rate, subsequently dissolution rate also decliness. A closed system can numerically be extrapolated as an open system with an infinitesimally slow flow rate. The kinetics of closed systems are orders of slower than open systems, which are far from equilibrium. Near equilibrium, coupled dissolution and precipitation is responsible for slow kinetics, which also explains the large difference in field and laboratory rates of dissolution (Zhu et al., 2004, 2009, 2010). Zhu et al. (2010) attempted to extrapolate a closed system (Ganor et al., 2007) to an open system through reactive transport modelling in 1D, assuming single clay precipitation along with primary mineral dissolution and reported time and space variability of saturation index (SI) of phases with constant dissolution and precipitation rate. The current study experimentally shows the possibility of multiple phases precipitation from single primary rock dissolution. The precipitation of multiple amorphous precursors and chemical evolution with increasing extent of dissolution poses substantial limitations for establishing r- ΔG_r relationship.

4.5. Geochemical implications

Basalt dissolution kinetics measured in laboratory experiments under open-system conditions have shown a few orders of faster rates for natural conditions, where the rate is measured using palagonite thickness (Gislason and Arnorsson, 1993; Gislason and Eugster, 1987b; Techer et al., 2001). This discrepancy in rate has been explained by long-time interaction in natural conditions (Parruzot et al., 2015). However,

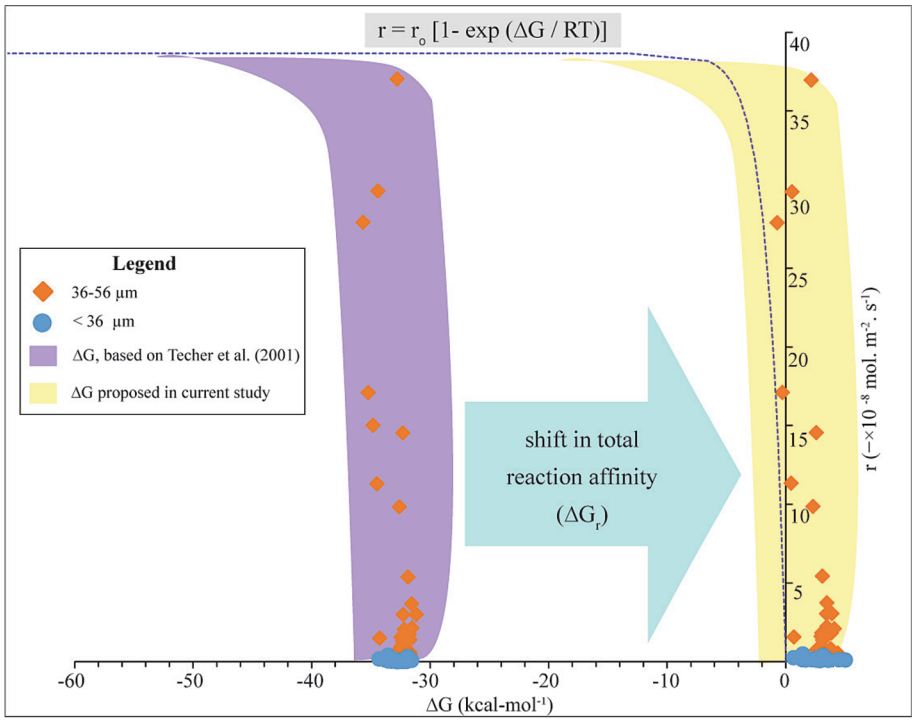

Fig. 8. Variation of total reaction affinity (ΔG_r) with dissolution rate (r) corresponding to each step of reaction. The dotted blue line indicates the expected theoretical trend between total reaction affinity and rate, according to transition state theory (TST). The orange diamond indicates an experiment with a 36–56 µm fraction of glass, and the blue circle indicates an experiment with < 36 µm glass. The greenish band showed the experimental data when reaction affinity was calculated according to the consideration in Techer et al. (2001), which results in a shift in ΔG_r in the negative direction. The yellow band shows the experimental points data when total reaction affinity was calculated considering brucite in equilibrium with the reacting solution and basalt.

the current study adds another possibility of basalt dissolution in a closed system within the natural terrain, as the rate lowers by two orders within 24 days. This study holds importance given many recent studies highlighting enhanced rock weathering of basalt as a potential strategy for CDR (Beearling et al., 2020, 2024; Goll et al., 2021; Viene et al.,2022).

4.5.1. *Impact of poor drainage on CDR potential by ERW of basalt*

Basalt dissolution rate in open systems with flow-rate high enough to maintain system far from equilibrium at steady state, remains higher. In contrast, the dissolution rate attains lower values with a decreasing flow rate. A closed system experiences an evolution in dissolution rates starting at a higher rate when the system approaches equilibrium or quasi-steady state, due to coupled dissolution and precipitation, the kinetics of dissolution lowers by two orders in 24 days. The total cations released by basalt glass dissolution increase at the same rate as glass dissolution until equilibrium is achieved and cations start fractionating in the precipitating phases. Any estimation based on total released cations due to basalt glass dissolution may give erroneous results if the equilibrium condition has not been investigated and precipitation-related correction is not incorporated. Large-scale estimation of CDR potential by ERW needs incorporation of factors that can affect amount of bivalent cations released by weathering. Beerling et al. (2024) estimated the CDR potential through field-based experiments, where total cation lost from basalt was considered available for bicarbonate formation. Although Beerling and others' calculation method accounts the effect of closed system kinetics evolution, as mass loss has been calculated from parent material, the fractionation of bivalent cation has not been considered. The current study shows within 20 h, magnesium starts fractionating in the secondary product, and after 54 h, calcium starts fractionating from the solution. We have calculated the projected amount of bivalent cations at each step of reaction if basalt dissolution is considered with evolving kinetics according to closed system, ignoring precipitation. We compared it with measured values of bivalent cations (see Appendix A. Supplementary material Section S6), which accounts both kinetics evolution as well as precipitation. The total amount of bivalent cations, after 400 h, remains 10 times lower than calculations-based estimation (see Fig. 9). Although this study signifies the importance of closed system-based calculations, it still cannot be strictly applied to any cropland, without soil textural information. The natural weathering regimes vary between an ideal closed system, poor drainage (full water storage) and an ideal open system, good drainage (full discharge). Hence, a realistic calculation of CDR potential by ERW of basalt glass in any cropland requires information about drainage system, which implies water residence time.

4.5.2. *Other implications of basalt glass alteration study in closed system*

The current study provides crucial laboratory evidence to the theoretical model proposed by Crovisier et al. (1992) for basalt alteration in a closed system in volcanic terrains like Iceland. Although the reaction advance did not reach the extent of zeolite formation, the mineralisation sequence supports the continuously evolving nature of 2:1 clay chemistry. This observation could explain the heterogeneity in the clay chemistry in soils having multiple dry and wet cycles in poor drainage, as the reaction will be reset to a new extent due to dilution each time. In volcanic terrains, a significant proportion of precipitation remains trapped as it percolates into fissures and joints or is confined to volcanic craters, calderas, and local depressions, resulting in lakes. Results of this study explain the nucleation pathways of neo-formation of clay in active volcanic fields where the basalt surface remains heated enough so that water does not evaporate, but interacts with basalt in the joints and fissures, paving the paths of secondary mineralisation, e.g. bole beds formed in Deccan provinces (Sriwastava et al., 2023). The experimental condition also helps understand the mineralisation pathways in alkaline lakes, which are reported as sites for prebiotic life (Toner and Catling, 2019, 2020). The information on element sequestration in secondary

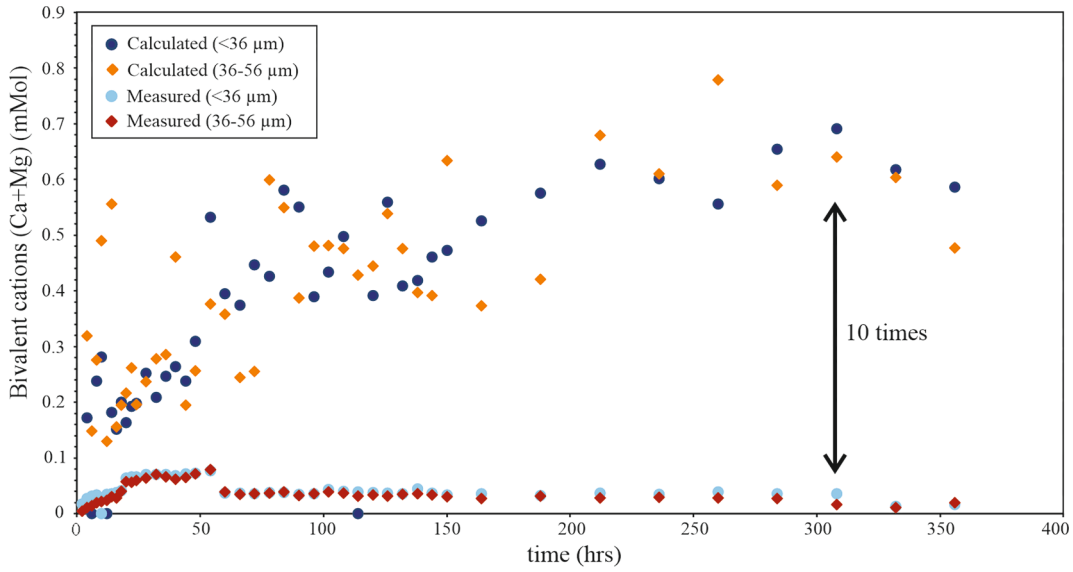

Fig. 9. Amount of bivalent cations (Ca + Mg) in fluid interacting with basalt glass in a closed system. Measured values are sum of the concentrations of Ca and Mg at each reaction step. The calculated amount of bivalent cations results when secondary precipitation is not considered, and total cations released from basalt are estimated from a normalised mass loss rate. The calculated values automatically incorporate effect of precipitation on rates of dissolution in closed system.

mineral nucleation over time greatly impacts the biogeochemistry of alkaline lake environment, especially microbialites formation, during the geochemical evolution of early earth. This study also holds importance for understanding the origin of clay rich beds in the volcanic terrains of Mars due to alteration of basaltic fragments (Treiman et al., 2015; Thorpe et al., 2022).

5. Conclusions

This study investigated basalt and water interaction at high time resolution (hour scale) under poor drainage conditions; our results show that nucleation of secondary products starts within 20 h of the onset of the reaction, thus paving the way for the initial surface nucleation. Brucite nucleation at an early stage indicates a strong control on the chemistry of honeycomb-shaped smectites that precipitated later. At geological time scale, such observation highlights the crucial importance of closed system (shorter duration) studies demonstrating the first step towards alteration reaction before the system continues as closed, open or mixed later. The cations released as a result of basalt glass dissolution may or may not be available for further utilisation in bicarbonate formation due to interruption by precipitation, affecting the potential of CDR by basalt dissolution in natural weathering regime. The major findings of this study are summarised as follows:

1) Within 20 h, brucite-like structures are the first secondary product that reaches precipitation during basalt glass alteration in a closed system, followed by 2:1 clay structure precursor, grown epitaxially over the sheet-like structure of brucite. This implies that the time required in a closed system to affect the pathway of any alteration reaction is very small at a geological time scale, suggesting the important role of a closed system at each site for alteration studies.
2) The initial dissolution rate in a closed system drops by 100 times in 24 days.
3) The total amount of measured bivalent cations, after 400 h of basalt glass dissolution in a closed system, remains 10 times lower than estimated values without considering precipitation, suggesting an overestimation of CRD potential by ERW of basalt.

Data availability:

Data are available through Mendeley Data at: https://doi.org/10.17632/vz78n3wwfb.1.

CRediT authorship contribution statement

Piyush Sriwastava: Writing – review & editing, Writing – original draft, Visualization, Project administration, Methodology, Investigation, Funding acquisition, Formal analysis, Data curation, Conceptualization. **Vijay Kumar Saini:** Writing – review & editing, Methodology, Investigation, Formal analysis, Data curation. **George Mathew:** Writing – review & editing, Validation, Supervision, Project administration. **Anil D. Shukla:** Writing – review & editing, Validation.

Declaration of competing interest

The authors declare that they have no known competing financial interests or personal relationships that could have appeared to influence the work reported in this paper.

Acknowledgements:

This work was supported by the Prime Minister Research Fellowship (PMRF) for PS. PS and GM thank Prof. Hetu Seth for providing the Hawaiian glass sample. PS and GM thank the Department of Earth Sciences and SAIF, IIT-Bombay, for their help in conducting analytical studies. GM thanks DST-FIST, Government of India, for funding FTIR. VKS thanks IIT-Bombay for completing part of the work during his M.Tech (Geo-exploration) programme. ADS expresses his appreciation towards PRL, Ahmedabad, for the support. PS and GM thank Department of Environmental Geosciences, University of Vienna, Austria, for BET analysis.

Appendix A. Supplementary material

Supplementary material to this article can be found online at https://doi.org/10.1016/j.gca.2025.01.042.

References

Aagaard, P., Helgeson, H.C., 1982. Thermodynamic and kinetic constraints on reaction rates among minerals and aqueous solutions; I, Theoretical Considerations. *American Journal of Science* 282 (3), 237–285.

Advocat, T., Chouchan, J.L., Crovisier, J.L., Guy, C., Daux, V., Jegou, C., Vernaz, E., 1997. Borosilicate nuclear waste glass alteration kinetics: chemical inhibition and affinity control. *MRS Online Proceedings Library (OPL)* 506, 63.

Alekseyev, V.A., Medvedeva, L.S., Prisyagina, N.I., Meshalkin, S.S., Balabin, A.I., 1997. Change in the dissolution rates of alkali feldspars as a result of secondary mineral precipitation and approach to equilibrium. *Geochimica et Cosmochimica Acta* 61 (6), 1125–1142.

Angeli, F., Gaillard, M., Jollivet, P., Charpentier, T., 2006. Influence of glass composition and alteration solution on leached silicate glass structure: a solid-state NMR investigation. *Geochimica et Cosmochimica Acta* 70 (10), 2577–2590.

Banfield, J.F., Jones, B.F., Veblen, D.R., 1991. An AEM-TEM study of weathering and diagenesis, Abert Lake, Oregon: II. Diagenetic modification of the sedimentary assemblage. *Geochimica et Cosmochimica Acta* 55 (10), 2795–2810.

Bas, M.L., Maitre, R.L., Streckeisen, A., Zanettin, B., 1986. A chemical classification of volcanic rocks based on the total alkali-silica diagram. *Journal of Petrology* 27 (3), 745–750. IUGS Subcommission on the Systematics of Igneous Rocks.

Beerling, D.J., Kantzas, E.P., Lomas, M.R., Wade, P., Eufrasio, R.M., Renforth, P., Banwart, S.A., 2020. Potential for large-scale CO2 removal via enhanced rock weathering with croplands. *Nature* 583 (7815), 242–248.

Beerling, D.J., Epihov, D.Z., Kantola, I.B., Masters, M.D., Reershemius, T., Planavsky, N. J., Banwart, S.A., 2024. Enhanced weathering in the US Corn Belt delivers carbon removal with agronomic benefits. *Proceedings of the National Academy of Sciences* 121 (9), e2319436121.

Berger, G., Claparols, C., Guy, C., Daux, V., 1994. Dissolution rate of a basalt glass in silica-rich solutions: implications for long-term alteration. *Geochimica et Cosmochimica Acta* 58 (22), 4875–4886.

Berger, G., Schott, J., Guy, C., 1988. Behaviour of Li, Rb and Cs during basalt glass and olivine dissolution and chlorite, smectite and zeolite precipitation from seawater: experimental investigations and modelisation between 50 and 300° C. *Chemical Geology* 71 (4), 297–312.

Berger, G., Schott, J., Loubet, M., 1987. Fundamental processes controlling the first stage of alteration of a basalt glass by seawater: an experimental study between 200 and 320° C. *Earth and Planetary Science Letters* 84 (4), 431–445.

Berner, R.A., 1978. Rate control of mineral dissolution under earth surface conditions. *American Journal of Science* 278 (9), 1235–1252.

Bettison-Varga, L., Mackinnon, I.D., 1997. The role of randomly mixed-layered chlorite/smectite in the transformation of smectite to chlorite. *Clays and Clay Minerals* 45, 506–516.

Bouakkaz, R., Abdelouas, A., El Mendili, Y., Grambow, B., Gin, S., 2016. SON68 glass alteration under Si-rich solutions at low temperature (35–90° C): kinetics, secondary phases and isotopic exchange studies. *Rsc Advances* 6 (76), 72616–72633.

Bourcier, W.L., Ebert, W.L., Feng, X., 1992. Modelling surface area to volume effects on borosilicate glass dissolution. *MRS Online Proceedings Library (OPL)* 294, 577.

Brown, K. (2011, May). Thermodynamics and kinetics of silica scaling. In *International Workshop on Mineral Scaling* (p. 8). Manila, Philippines.

Chakoumakos, B.C., Loong, C.K., Schultz, A.J., 1997. Low-temperature structure and dynamics of brucite. *The Journal of Physical Chemistry B* 101 (46), 9458–9462.

Christidis, G.E., 2006. Genesis and compositional heterogeneity of smectites. Part III: Alteration of basic pyroclastic rocks—A case study from the Troodos Ophiolite Complex, Cyprus. *American Mineralogist* 91 (4), 685–701.

Crovisier, J.L., Honnorez, J., Eberhart, J.P., 1987. Dissolution of basaltic glass in seawater: mechanism and rate. *Geochimica et Cosmochimica Acta* 51 (11), 2977–2990.

Crovisier, J.L., Advocat, T., Petit, J.C., Fritz, B., 1988a. Alteration of basaltic glass in Iceland as a natural analogue for nuclear waste glasses: geochemical modelling with DISSOL. *MRS Online Proceedings Library (OPL)* 127, 57.

Crovisier, J.L., Atassi, H., Daux, V., Honnorez, J., Petit, J.C., Eberhart, J.P., 1988b. A new insight into the nature of the leached layers formed on basaltic glasses in relation to the choice of constraints for long term modelling. *MRS Online Proceedings Library (OPL)* 127, 41.

Crovisier, J.L., Daux, V., 1990. Populations of clays formed by alteration of subglacial hyaloclastites from Iceland. *Chemical Geology* 84 (1–4), 261–263.

Crovisier, J.L., Advocat, T., Dussossoy, J.L., 2003. Nature and role of natural alteration gels formed on the surface of ancient volcanic glasses (Natural analogs of waste containment glasses). *Journal of Nuclear Materials* 321 (1), 91–109.

Crovisier, J.L., Honnorez, J., Fritz, B., Petit, J.C., 1992. Dissolution of subglacial volcanic glasses from Iceland: laboratory study and modelling. *Applied Geochemistry* 7, 55–81.

Cuadros, J., Afsin, B., Jadubansa, P., Ardakani, M., Ascaso, C., Wierzchos, J., 2013. Microbial and inorganic control on the composition of clay from volcanic glass alteration experiments. *American Mineralogist* 98 (2–3), 319–334.

Curti, E., Crovisier, J.L., Morvan, G., Karpoff, A.M., 2006. Long-term corrosion of two nuclear waste reference glasses (MW and SON68): a kinetic and mineral alteration study. *Applied Geochemistry* 21 (7), 1152–1168.

Daux, V., Crovisier, J.L., Hemond, C., Petit, J.C., 1994. Geochemical evolution of basaltic rocks subjected to weathering: fate of the major elements, rare earth elements, and thorium. *Geochimica et Cosmochimica Acta* 58 (22), 4941–4954.

Daux, V., Guy, C., Advocat, T., Crovisier, J.L., Stille, P., 1997. Kinetic aspects of basaltic glass dissolution at 90° C: role of aqueous silicon and aluminium. *Chemical Geology* 142 (1–2), 109–126.

De La Fuente, S., Cuadros, J., Fiore, S., Linares, J., 2000. Electron microscopy study of volcanic tuff alteration to illite-smectite under hydrothermal conditions. *Clays and Clay Minerals* 48 (3), 339–350.

Decarreau, A., Vigier, N., Pálková, H., Petit, S., Vieillard, P., Fontaine, C., 2012. Partitioning of lithium between smectite and solution: an experimental approach. *Geochimica et Cosmochimica Acta* 85, 314–325.

Declercq, J., Diedrich, T., Perrot, M., Gislason, S.R., Oelkers, E.H., 2013. Experimental determination of rhyolitic glass dissolution rates at 40–200° C and 2< pH< 10.1. *Geochimica et Cosmochimica Acta* 100, 251–263.

Dehouck, E., McLennan, S.M., Meslin, P.Y., Cousin, A., 2014. Constraints on abundance, composition, and nature of X-ray amorphous components of soils and rocks at Gale crater, Mars. *Journal of Geophysical Research: Planets* 119 (12), 2640–2657.

Dessert, C., Dupré, B., François, L.M., Schott, J., Gaillardet, J., Chakrapani, G., Bajpai, S., 2001. Erosion of Deccan Traps determined by river geochemistry: impact on the global climate and the $^{87}Sr/^{86}Sr$ ratio of seawater. *Earth and Planetary Science Letters* 188 (3–4), 459–474.

Dessert, C., Dupré, B., Gaillardet, J., François, L.M., Allègre, C.J., 2003. Basalt weathering laws and the impact of basalt weathering on the global carbon cycle. *Chemical Geology* 202 (3–4), 257–273.

Eggleton, R.A., Foudoulis, C., Varkevisser, D., 1987. Weathering of basalt: changes in rock chemistry and mineralogy. *Clays and Clay Minerals* 35, 161–169.

Fang, Q., Lu, A., Hong, H., Kuzyakov, Y., Algeo, T.J., Zhao, L., Chorover, J., 2023. Mineral weathering is linked to microbial priming in the critical zone. *Nature Communications* 14 (1), 345.

Fiore, S., Huertas, F.J., Huertas, F., Linares, J., 2001. Smectite formation in rhyolitic obsidian as inferred by microscopic (SEM-TEM-AEM) investigation. *Clay Minerals* 36 (4), 489–500.

Fox, L.E., 1988. The solubility of colloidal ferric hydroxide and its relevance to iron concentrations in river water. *Geochimica et Cosmochimica Acta* 52 (3), 771–777.

Frings, P.J., Buss, H.L., 2019. The central role of weathering in the geosciences. *Elements: an International Magazine of Mineralogy, Geochemistry, and Petrology* 15 (4), 229–234.

Ghiara, M.R., Franco, E., Petti, C., Stanzione, D., Valentino, G.M., 1993. Hydrothermal interaction between basaltic glass, deionized water and seawater. *Chemical Geology* 104 (1–4), 125–138.

Gin, S., Ryan, J.V., Schreiber, D.K., Neeway, J., Cabié, M., 2013. Contribution of atom-probe tomography to a better understanding of glass alteration mechanisms: Application to a nuclear glass specimen altered 25 years in a granitic environment. *Chemical Geology* 349, 99–109.

Gislason, S.R., Arnórsson, S., 1993. Dissolution of primary basaltic minerals in natural waters: saturation state and kinetics. *Chemical Geology* 105 (1–3), 117–135.

Gislason, S.R., Eugster, H.P., 1987a. Meteoric water-basalt interactions. I: A laboratory study. *Geochimica et Cosmochimica Acta* 51 (10), 2827–2840.

Gislason, S.R., Eugster, H.P., 1987b. Meteoric water-basalt interactions. II: A field study in NE Iceland. *Geochimica et Cosmochimica Acta* 51 (10), 2841–2855.

Gislason, S.R., Oelkers, E.H., 2003. Mechanism, rates, and consequences of basaltic glass dissolution: II. An experimental study of the dissolution rates of basaltic glass as a function of pH and temperature. *Geochimica et Cosmochimica Acta* 67 (20), 3817–3832.

Goll, D.S., Ciais, P., Amann, T., Buermann, W., Chang, J., Eker, S., Vicca, S., 2021. Potential CO2 removal from enhanced weathering by ecosystem responses to powdered rock. *Nature Geoscience* 14 (8), 545–549.

Grambow, B., Jercinovic, M.J., Ewing, R.C., Byers, C.D., 1985. Weathered basalt glass: a natural analogue for the effects of reaction progress on nuclear waste glass alteration. *MRS Online Proceedings Library (OPL)* 50, 263.

Guy, C., Schott, J., 1989. Multisite surface reaction versus transport control during the hydrolysis of a complex oxide. *Chemical Geology* 78 (3–4), 181–204.

Heřmanská, M., Voigt, M.J., Marieni, C., Declercq, J., Oelkers, E.H., 2023. A comprehensive and consistent mineral dissolution rate database: part II: secondary silicate minerals. *Chemical Geology* 636, 121632.

Keller, W.D., Reynolds, R.C., Inoue, A., 1986. Morphology of clay minerals in the smectite-to-illite conversion series by scanning electron microscopy. *Clays and Clay Minerals* 34, 187–197.

Kump, L.R., Brantley, S.L., Arthur, M.A., 2000. Chemical weathering, atmospheric CO_2, and climate. *Annual Review of Earth and Planetary Sciences* 28 (1), 611–667.

Lasaga, A.C., Soler, J.M., Ganor, J., Burch, T.E., Nagy, K.L., 1994. Chemical weathering rate laws and global geochemical cycles. *Geochimica et Cosmochimica Acta* 58 (10), 2361–2386.

Leturcq, G., Berger, G., Advocat, T., Vernaz, E., 1999. Initial and long-term dissolution rates of aluminosilicate glasses enriched with Ti. Zr and Nd. *Chemical Geology* 160 (1–2), 39–62.

Loock, S., Van Wyk de Vries, B., Hénot, J.M., 2010. Clinker formation in basaltic and trachybasaltic lava flows. *Bulletin of Volcanology* 72, 859–870.

Meng, J., Liu, X., Li, B., Zhang, J., Hu, D., Chen, J., Shi, W., 2018. Conversion reactions from dioctahedral smectite to trioctahedral chlorite and their structural simulations. *Applied Clay Science* 158, 252–263.

Meunier, A., Petit, S., Cockell, C.S., El Albani, A., Beaufort, D., 2010. The Fe-rich clay microsystems in basalt-komatiite lavas: importance of Fe-smectites for pre-biotic molecule catalysis during the Hadean eon. *Origins of Life and Evolution of Biospheres* 40 (3), 253–272.

Murphy, W.M., Oelkers, E.H., Lichtner, P.C., 1989. Surface reaction versus diffusion control of mineral dissolution and growth rates in geochemical processes. *Chemical Geology* 78 (3–4), 357–380.

Nagy, K.L., Lasaga, A.C., 1992. Dissolution and precipitation kinetics of gibbsite at 80° C and pH 3: The dependence on solution saturation state. *Geochimica et Cosmochimica Acta* 56 (8), 3093–3111.

Nagy, K.L., Blum, A.E., Lasaga, A.C., 1991. Dissolution and precipitation kinetics of kaolinite at 80° C and pH 3; the dependence on solution saturation state. *American Journal of Science* 291 (7), 649–686.

Neeway, J.J., Kerisit, S.N., Liu, J., Zhang, J., Zhu, Z., Riley, B.J., Ryan, J.V., 2016. Ion-exchange interdiffusion model with potential application to long-term nuclear waste glass performance. *The Journal of Physical Chemistry C* 120 (17), 9374–9384.

Nesbitt, H.W., Wilson, R.E., 1992. Recent chemical weathering of basalts. American *Journal of Science* 292 (10), 740–777.

Oelkers, E.H., Gislason, S.R., 2001. The mechanism, rates and consequences of basaltic glass dissolution: I. An experimental study of the dissolution rates of basaltic glass as a function of aqueous Al, Si and oxalic acid concentration at 25° C and pH= 3 and 11. *Geochimica et Cosmochimica Acta* 65 (21), 3671–3681.

Parkhurst, D.L., Appelo, C.A.J., 1999. User's guide to PHREEQC (Version 2): A computer program for speciation, batch-reaction, one-dimensional transport, and inverse geochemical calculations. *Water-Resources Investigations Report* 99 (4259), 312.

Parruzot, B., Jollivet, P., Rébiscoul, D., Gin, S., 2015. Long-term alteration of basaltic glass: Mechanisms and rates. *Geochimica et Cosmochimica Acta* 154, 28–48.

Paul, A., 1977. Chemical durability of glasses; a thermodynamic approach. *Journal of Materials Science* 12, 2246–2268.

Rinder, T., von Hagke, C., 2021. The influence of particle size on the potential of enhanced basalt weathering for carbon dioxide removal-Insights from a regional assessment. *Journal of Cleaner Production* 315, 128178.

Rowe, M.C., Brewer, B.J., 2018. AMORPH: A statistical program for characterizing amorphous materials by X-ray diffraction. *Computers & Geosciences* 120, 21–31.

Schuiling, R.D., Krijgsman, P., 2006. Enhanced weathering: an effective and cheap tool to sequester CO_2. *Climatic Change* 74 (1), 349–354.

Shannon, R.D., 1976. Revised effective ionic radii and systematic studies of interatomic distances in halides and chalcogenides. *Acta Crystallographica Section a: Crystal Physics, Diffraction, Theoretical and General Crystallography* 32 (5), 751–767.

Spanos, N., Koutsoukos, P.G., 1998. Kinetics of precipitation of calcium carbonate in alkaline pH at constant supersaturation. Spontaneous and seeded growth. *The Journal of Physical Chemistry B* 102 (34), 6679–6684.

Sriwastava, P., Singh, V.V., Mathew, G., Kogure, T., Myneni, S., 2023. Origin of clays in the interbasaltic red boles of Deccan Volcanics: Pedogenesis versus palagonitization. *Applied Clay Science* 246, 107183.

Stefánsson, A., Gíslason, S.R., 2001. Chemical weathering of basalts, Southwest Iceland: effect of rock crystallinity and secondary minerals on chemical fluxes to the ocean. *American Journal of Science* 301 (6), 513–556.

Strefler, J., Amann, T., Bauer, N., Kriegler, E., Hartmann, J., 2018. Potential and costs of carbon dioxide removal by enhanced weathering of rocks. *Environmental Research Letters* 13 (3), 034010.

Taylor, L.L., Driscoll, C.T., Groffman, P.M., Rau, G.H., Blum, J.D., Beerling, D.J., 2020. Increased carbon capture by a silicate-treated forested watershed affected by acid deposition. *Biogeosciences Discussions* 2020, 1–29.

Techer, I., Advocat, T., Lancelot, J., Liotard, J.M., 2001. Dissolution kinetics of basaltic glasses: control by solution chemistry and protective effect of the alteration film. *Chemical Geology* 176 (1–4), 235–263.

Techner, I., Advocat, T., Vernaz, E., Lancelot, J.R., Liotard, J.M., 1998. Dissolution rate equations for basaltic glasses. Comparison with experimental data. *Mineral Mag A* 62, 1498–1499.

Thorpe, M.T., Bristow, T.F., Rampe, E.B., Tosca, N.J., Grotzinger, J.P., Bennett, K.A., Achilles, C.N., Blake, D.F., Chipera, S.J., Downs, G., Downs, R.T., Morrison, S.M., Tu, V., Castle, N., Craig, P., Marais, D.J.D., Hazen, R.M., Ming, D.W., Morris, R.V., Treiman, A.H., Vaniman, D.T., Yen, A.S., Vasavada, A.R., Dehouck, E., Bridges, J.C., Berger, J., McAdam, A., Peretyazhko, T., Siebach, K.L., Bryk, A.B., Fox, V.K., Fedo, C. M., 2022. Mars Science Laboratory CheMin data from the Glen Torridon region and the significance of lake-groundwater interactions in interpreting mineralogy and sedimentary history. *Journal of Geophysical Research: Planets* 127 (11), e2021JE007099.

Toner, J.D., Catling, D.C., 2019. Alkaline lake settings for concentrated prebiotic cyanide and the origin of life. *Geochimica et Cosmochimica Acta* 260, 124–132.

Toner, J.D., Catling, D.C., 2020. A carbonate-rich lake solution to the phosphate problem of the origin of life. *Proceedings of the National Academy of Sciences* 117 (2), 883–888.

Treiman, A.H., Bish, D.L., Vaniman, D.T., Chipera, S.J., Blake, D.F., Ming, D.W., Morris, R.V., Bristow, T.F., Morrison, S.M., Baker, M.B., Rampe, E.B., Downs, R.T., Filiberto, J., Glazner, A.F., Gellert, R., Thompson, L.M., Schmidt, M.E., Deit, L.L., Weins, R.C., McAdam, A.C., Achilles, C.N., Edgett, K.S., Farmer, J.D., Fendrich, K.V., Grotzinger, J.P., Gupta, S., Morookian, J.M., Newcomb, M.E., Rice, M.S., Spray, J.G., Stolper, E.M., Sumner, D.Y., Vaavada, A.R., Yen, A.S., 2016. Mineralogy, provenance, and diagenesis of a potassic basaltic sandstone on Mars: ChemMin X-rat diffraction of the Windjana sample (Kimberley area, Gale Crater). *Journal of Geophysics Research: Planets* 121 (1), 75–106.

Tsipursky, S.I., Drits, V.A., 1984. The distribution of octahedral cations in the 2: 1 layers of dioctahedral smectites studied by oblique-texture electron diffraction. *Clay Minerals* 19 (2), 177–193.

Velde, B.B., Meunier, A., 2008. The origin of clay minerals in soils and weathered rocks. Springer Science & Business Media.

Vernaz, E., Gin, S., Jégou, C., Ribet, I., 2001. Present understanding of R7T7 glass alteration kinetics and their impact on long-term behavior modeling. *Journal of Nuclear Materials* 298 (1–2), 27–36.

Vienne, A., Poblador, S., Portillo-Estrada, M., Hartmann, J., Ijiehon, S., Wade, P., Vicca, S., 2022. Enhanced weathering using basalt rock powder: carbon sequestration, co-benefits and risks in a mesocosm study with Solanum tuberosum. *Frontiers in Climate* 4, 869456.

Wojdyr, M., 2010. Fityk: a general-purpose peak fitting program. *Journal of Applied Crystallography* 43 (5), 1126–1128.

Wolff-Boenisch, D., Gislason, S.R., Oelkers, E.H., Putnis, C.V., 2004. The dissolution rates of natural glasses as a function of their composition at pH 4 and 10.6, and temperatures from 25 to 74 C. *Geochimica et Cosmochimica Acta* 68 (23), 4843–4858.

Zhu, C., Blum, A.E., Veblen, D.R., 2004. Feldspar dissolution rates and clay precipitation in the Navajo aquifer at Black Mesa, Arizona, USA. *Water-Rock Interaction* 11, 895–899.

Zhu, C., Lu, P., 2009. Alkali feldspar dissolution and secondary mineral precipitation in batch systems: 3. Saturation states of product minerals and reaction paths. *Geochimica et Cosmochimica Acta* 73 (11), 3171–3200.

Zhu, C., Lu, P., Zheng, Z., Ganor, J., 2010. Coupled alkali feldspar dissolution and secondary mineral precipitation in batch systems: 4. Numerical modeling of kinetic reaction paths. *Geochimica et Cosmochimica Acta* 74 (14), 3963–3983.